

Micro-scale isotopic variability of low-temperature pyrite in fractured crystalline bedrock — A large Fe isotope fractionation between Fe(II)aq/pyrite and absence of Fe-S isotope co-variation

Yu, C.; Drake, H.; Lopez Fernandez, M.; Whitehouse, M.; Dopson, M.; Åström, M. E.;

Originally published:

May 2019

Chemical Geology 522(2019), 192-207

DOI: <https://doi.org/10.1016/j.chemgeo.2019.05.026>

Perma-Link to Publication Repository of HZDR:

<https://www.hzdr.de/publications/Publ-29315>

Release of the secondary publication
on the basis of the German Copyright Law § 38 Section 4.

CC BY-NC-ND

Micro-scale isotopic variability of low-temperature pyrite in fractured crystalline bedrock — a large Fe isotope fractionation between Fe(II)_{aq}/pyrite and absence of Fe-S isotope co-variation

Changxun Yu^{a*}, Henrik Drake^a, Margarita Lopez-Fernandez^b, Martin Whitehouse^c, Mark Dopson^b, Mats E. Åström^a

^aDepartment of Biology and Environmental Science, Linnaeus University, SE-39182 Kalmar, Sweden

^bCentre for Ecology and Evolution in Microbial Model Systems (EEMiS), Linnaeus University, SE-39182 Kalmar, Sweden

^cLaboratory for Isotope Geology, Swedish Museum of Natural History, P.O. Box 50 007, SE-10405 Stockholm, Sweden

*Corresponding author

Email: changxun.yu@lnu.se; yuchangxun2006@163.com

Phone: +46-737-539543

ABSTRACT

This study assessed Fe-isotope ratio (⁵⁶Fe/⁵⁴Fe, expressed as δ⁵⁶Fe relative to the IRMM-014 standard) variability and controls in pyrite that has among the largest reported S-isotope variability (maximum δ³⁴S: 140‰). The pyrite occurs as fine-grained secondary crystals in fractures throughout the upper kilometer of granitoids of the Baltic Shield, and was analyzed here for δ⁵⁶Fe by *in situ* secondary ion mass spectrometry (SIMS). Part of these pyrite crystals were picked from borehole instrumentation at depths of more than 400 m below sea level (m.b.s.l.), and thus are modern (known to have formed within 17 years) and can be compared with the δ⁵⁶Fe of the source dissolved ferrous iron. The δ⁵⁶Fe values of the modern pyrite crystals (-1.81‰ to +2.29‰) varied to a much greater extent than those of the groundwaters from which they formed (-0.48‰ to +0.13‰), providing strong field evidence for a large Fe

isotope fractionation during the conversion of $\text{Fe(II)}_{\text{aq}}$ to FeS and ultimately to pyrite. Enrichment of ^{56}Fe in pyrite relative to the groundwater was explained by equilibrium $\text{Fe(II)}_{\text{aq}}\text{-FeS}$ isotope fractionation, whereas depletion of ^{56}Fe in pyrite relative to the groundwater was mainly the result of sulfidization of magnetite and kinetic isotopic fractionation during partial transformation of micro-sized FeS to pyrite. In many pyrite crystals, there is an increase in $\delta^{34}\text{S}$ from crystal center to rim reflecting Rayleigh distillation processes (reservoir effects) caused by the development of closed-system conditions in the micro-environment near the growing crystals. A corresponding center-to-rim feature was not observed for the $\delta^{56}\text{Fe}$ values. It is therefore unlikely that the groundwater near the growing pyrite crystals became progressively enriched in the heavy Fe isotope, in contrast to what has been found for the sulfur in sulfate. Other pyrite crystals formed following bacterial sulfate reduction in the time period of mid-Mesozoic to Quaternary, had an almost identical Fe-isotope variability (total range: -1.50‰ to $+2.76\text{‰}$), frequency-distribution pattern, and relationship with $\delta^{34}\text{S}$ as the recent pyrite formed on the borehole instrumentation. These features suggest that fundamental processes are operating and governing the Fe-isotope composition of pyrite crystals formed in fractured crystalline bedrock over large time scales.

KEYWORDS: pyrite; iron isotopes; equilibrium Fe-isotope fractionation; magnetite sulfidization; partial pyritization; fractured crystalline bedrock

1. INTRODUCTION

Pyrite is thermodynamically the most stable form of iron sulfide (Berner, 1967) and thus, acts as the ultimate sink for dissolved ferrous iron and sulfide (H_2S) under reducing conditions in low-temperature subsurface environments. In these anoxic systems, the fractionation of the sulfur isotope ratio ($^{34}\text{S}/^{32}\text{S}$, expressed as $\delta^{34}\text{S}$ relative to the V-CDT standard) mainly occurs

during organoclastic sulfate reduction mediated by sulfate reducing bacteria (SRB) (Canfield, 2001; Detmers et al., 2001; Leavitt et al., 2013) or sulfate-driven anaerobic oxidation of methane mediated by a consortium of methanotrophic archaea and SRB (Hinrichs et al., 1999; Boetius et al., 2000; Lin et al., 2016). Accordingly, $\delta^{34}\text{S}$ variation in low-temperature pyrite is mainly governed by bacterial activities and extracellular conditions such as the availability of sulfate and electron donors (Ries et al., 2009; Drake et al., 2013; Lin et al., 2016; Lin et al., 2017).

The variation of the Fe-isotope ratio ($^{56}\text{Fe}/^{54}\text{Fe}$, expressed as $\delta^{56}\text{Fe}$ relative to the IRMM-014 standard) in low-temperature pyrite has been used to trace (i) modern and ancient microbial metabolisms (Archer and Vance, 2006; Johnson et al., 2008; Yoshiya et al., 2015); (ii) redox evolution of the oceans and atmosphere (Rouxel et al., 2005; Johnson et al., 2008; Fabre et al., 2011; Zhang et al., 2015); and (iii) Fe sources and cycling in sedimentary environments (Johnson et al., 2008; Virtasalo et al., 2013, 2015; Marin-Carbonne et al., 2014; Yoshiya et al., 2015). Nevertheless, the fractionation of $\delta^{56}\text{Fe}$ during the formation of low-temperature pyrite is not well constrained, which is mainly attributed to the fact that the interactions of Fe-bearing minerals with various inorganic, organic, and biotic processes can lead to strong enrichments of either heavy or light Fe isotopes in $\text{Fe(II)}_{\text{aq}}$ pools relative to the source minerals (Beard, 1999; Bullen et al., 2001; Icopini et al., 2004; Brantley et al., 2004; Balci et al., 2006; Crosby et al., 2007; Chapman et al., 2009; Mikutta et al., 2009; Kiczka et al., 2010). By analyzing $\delta^{56}\text{Fe}$ of both the pyrite and the $\text{Fe(II)}_{\text{aq}}$ from which the pyrite was derived, the isotope-fractionation processes involved in the production of $\text{Fe(II)}_{\text{aq}}$ can be ruled out, allowing a better assessment of the Fe-isotope fractionation processes during transfer of $\text{Fe(II)}_{\text{aq}}$ to FeS and eventually to pyrite. Under field conditions, no such study has yet been carried out, which is partly due to the fact that the pyrite crystals investigated in most studies were formed a long time ago and thus, are not directly comparable with the present solutions

(groundwaters), and partly to the difficulty in sampling representative groundwaters from the system in which pyrite crystals precipitated.

This study focuses on the fracture system in the upper kilometer of granitoids of the Baltic Shield in an area in southeastern Sweden (the Laxemar area and the Äspö Hard Rock Laboratory abbreviated as “Äspö HRL”), where microscale variability in $\delta^{34}\text{S}$ has been reported for (i) pyrite crystals of low-temperature origin, formed in mid-Mesozoicum to Quaternary times in the fracture systems (hereafter “fracture pyrite”); and (ii) <17 years old crystals precipitated on borehole instrumentation in five borehole sections at >400 m depth at the Äspö HRL (“modern pyrite”). Both fracture and modern pyrite displayed among the largest reported variability in $\delta^{34}\text{S}$, which exceeds 140‰ and 100‰, respectively, in maximum and 103‰ and 60‰, respectively, within individual crystals (Drake et al., 2013, 2015a,b). This substantial intra- and inter- crystal variation, in particular the progressive increase in $\delta^{34}\text{S}$ values from interiors to rims in many crystals, is interpreted to reflect the progressive exhaustion of sulfate following a Rayleigh distillation process near the growing pyrite crystals (Drake et al., 2013, 2015b). Here we revisited the pyrite crystals and determined $\delta^{56}\text{Fe}$ values as close as possible to the spots for which $\delta^{34}\text{S}$ data exist. The data was further coupled to Fe-isotopic and microbial-community composition in the groundwaters residing in the fracture system. This is the first study to investigate Fe isotope variability and controls in both modern and ancient pyrite derived from a deep terrestrial environment. The aims of this study were to (i) investigate Fe-isotope fractionation processes during the transfer of $\text{Fe(II)}_{\text{aq}}$ to pyrite under field conditions; (ii) determine whether the Fe isotopes co-vary with the S isotopes, and thus may be controlled by similar mechanisms; and (iii) assess whether the modern pyrite formed on borehole instrumentation in a short period under well-defined conditions have similar Fe-isotope features as the much older (fracture) pyrite dispersed throughout the fracture system.

2. SETTING, BOREHOLE LAYOUT, AND LOGGING

The Laxemar area and Äspö HRL are located in the coastal area of southeastern Sweden (Fig. 1a). The bedrock is dominated by 1.8-1.85 Ga granitoids and diorite/gabbro of the Transscandinavian Igneous Belt (Wahlgren et al., 2008). Regional deformation zones (surface trace lengths >1000 m, thicknesses of 10-150 m), minor deformation zones (surface trace lengths <1000 m, thicknesses <10 m), and a variety of open and sealed single fractures occur in the bedrock (Wahlgren et al., 2008). The open fractures vary widely in frequency and thickness among the deformation zones, but typically the cores of the zones are most extensively fractured with 10-20 fractures per meter (Munier, 2004).

The fractures are coated with a variety of minerals in variable proportions. These include chlorite, smectite, illite, corrensite, illite- or chlorite-dominated mixed-layer clays, calcite, pyrite, Fe-oxides, epidote, feldspar, quartz, prehnite, gypsum, and zeolites (Drake et al., 2009; Dideriksen et al., 2010). A study on the vertical distribution of redox-sensitive minerals (e.g. pyrite and goethite) and U-series disequilibrium in the fracture network of the Laxemar area indicates that the present redox front in the bedrock is located between 15-55 m below the ground surface (Drake et al., 2009). Oxygenated water may have infiltrated down to 110 m during deglaciation, as evidenced by the presence of well-crystalline Fe-oxides of low-temperature origin to these depths (Dideriksen et al., 2010). The groundwater in the fracture network is heterogeneous with large inter-fracture variability in concentrations of major ions and isotopic composition of H₂O (Mathurin et al., 2012; Gimeno et al., 2014). This is explained by a range of sources and ages of the waters and only partial connectivity among the fractures and fractures zones (Mathurin et al., 2012).

Two boreholes, in focus in this study (KA3105A referred to as “A” and KA3385A referred to as “B”), were drilled sub-horizontally into the bedrock from the Äspö HRL tunnel

wall in 1994 to early 1995 at 415 and 445 m.b.s.l., respectively (Fig. 1b) (Drake et al., 2015b). Along each borehole, single or clusters of multiple fractures were enclosed by inflatable packers of rubber on acid-proof stainless steel frames (containing Fe, Cr, Ni, Mn, Mo, Nb, and Ti) attached to an Al connecting pipe (with a diameter of 2 cm). This created borehole sections (packed-off fractures) with defined volumes (A2, A3, A4, B1, and B2, Fig. 1c-e, Table 1). Each section is connected to a panel in the Äspö HRL tunnel wall via polyamide tubing through which groundwater from the section can be extracted by opening the borehole valve. The tubing is fastened to the Al pipe with black PVC tape about every 30 cm (Fig. 1e). The PVC material may contain up to 65% plasticizers.

3. MATERIAL AND METHODS

3.1. Pyrite

In January 2012, the instrumentation in each of the five borehole sections was withdrawn (Fig. 1c-e) and immediately visually inspected for physical appearance and secondary precipitates (for details, see Drake et al. (2015b)). Thereafter, mineral precipitates were scraped off from the borehole instrumentation using a chisel and tweezers and immediately stored in sample bags flushed with N₂ gas. The sample bags were then vacuum pumped and sealed using a heating device before storage in an Al-coated sample bag from which oxygen was evacuated. After this, the equipment was re-installed in the boreholes. A total of 47 pyrite crystals were hand-picked from the mineral precipitates obtained from the five borehole sections (Table A1). These pyrite crystals precipitated over the time period during which the instrumentation was in the boreholes, i.e. in 1995-2012 that makes them a maximum of 17 years old.

A total of 110 fracture pyrite crystals were sampled from 42 pyrite-bearing open fractures (1-7 crystals from each of the fractures) at depths between 2 and 859 m.b.s.l in drill cores from the Laxemar area (Drake et al., 2013, 2015a) (Table A2). These pyrite-bearing fractures

carry calcite that is co-genetic with pyrite and expresses stable isotopic signatures indicative of low-temperature formation conditions in mid-Mesozoic to Quaternary (Drake et al., 2013), and consist of an approximately equal number of (i) low-water flow single fractures located outside fracture zones ($< 3 \times 10^{-9} \text{ m}^2 \text{ s}^{-1}$); (ii) low-water flow fractures within fracture zones ($< 3 \times 10^{-9} \text{ m}^2 \text{ s}^{-1}$); and (iii) high-water flow fractures with dominantly large apertures within fracture zones (up to $\sim 8 \times 10^{-5} \text{ m}^2 \text{ s}^{-1}$) (Drake et al., 2013). All drill cores were obtained by the triple-tube drilling technique (Ask et al., 2005), which protects the cores from rotation, fragmentation, and flushing water and thus, maintains the fragile minerals on the fracture surface intact (Drake et al., 2013).

The crystal habit, appearance (e.g., euhedral/subhedral/anhedral) and grain size of pyrite crystals plus their paragenetic minerals in precipitates scraped off from borehole instrumentation were examined with a stereomicroscope and Scanning Electron Microscope equipped with an Energy Dispersive Spectrometer (SEM-EDS) in low-vacuum mode as previously described (Drake et al., 2013, 2015b). Thereafter, the pyrite crystals were hand-picked under the stereomicroscope and mounted in epoxy, which was polished until the crystal interiors were exposed. The pyrite crystals in the polished epoxy-pucks (pucks 1-4, Fig. A3-A6) were then investigated again with the SEM to identify any zonation, cracks, and impurities. Only the crystals with a Fe/S molar ratio of nearly 0.5 were included in subsequent SIMS measurements. In addition, the scraped-off precipitates from which pyrite crystals had been picked were mounted in epoxy. After polishing until the mineral grain interiors were exposed, the mineralogical composition and morphological characteristics (i.e. crystal habit, overgrowths, and zonations) were investigated with SEM-EDS and reflective light microscope

The $\delta^{56}\text{Fe}$ of the pyrite crystals were measured by the SIMS technique in four sessions using a Cameca IMS1280 ion microprobe at NordSIM, Swedish Museum of Natural History,

Stockholm. Intra-crystal transects with up to twelve and fourteen spots were conducted for the modern and fracture pyrite crystals, respectively (Table A1, A2). The analytical procedures and instrument parameters were similar to those described elsewhere (Virtasalo et al., 2015). A -13 kV O₂⁻ primary beam of ~2 nA intensity was focused to a spot of about 10 μm. Analyses were performed in automated sequences, with each analysis comprising successively of a 90 s pre-sputtering to remove the gold coating over a rastered 25×25 μm area, centering of the secondary beam in the field aperture to correct for small surface relief, and data acquisition in 16×4 s integrations. Partially missed spots observed by SEM or with too deviating sample/standard count ratio (below 0.70) were not considered for further interpretation. Secondary ion signals of ⁵⁴Fe⁺ and ⁵⁶Fe⁺ were simultaneously detected using two Faraday detectors. To monitor any potential isobaric interference on ⁵⁴Fe from ⁵⁴Cr, ⁵²Cr⁺ was also measured in an ion counting electron multiplier; the levels were negligible in all samples. All detectors were operated at a mass resolution (M/ΔM) of 2560. The Balmat pyrite standard ($\delta^{56}\text{Fe} = -0.40 \pm 0.04\%$, 2σ, Whitehouse and Fedo, (2007)) was measured regularly between the determinations on pyrite crystals in epoxy-pucks 1-4. The Balmat measurements in each session were used to determine a small linear drift correction (if necessary). The internal precision for each session was better than ±0.11‰ (1σ), while external reproducibility based on the Balmat measurements in each session (Table A7) was better than ±0.12‰ (1σ).

3.2. Groundwater

As part of the Swedish Nuclear Fuel and Waste Management Company's (SKB) site investigation and long-term monitoring programs, two slightly different groundwaters from the packed-off bedrock fractures have been sampled by onsite SKB geochemists. "Stagnant groundwater" was extracted immediately after opening the borehole valve and represents water that has been in contact with and thus, may be affected by the instrumentation materials.

“Pristine groundwater” was sampled after discharge (through an open valve) of a water volume corresponding to at least ten borehole-section volumes and thus, represents water residing and flowing in the bedrock fractures and unaffected by the instrumentation materials. The anoxic conditions of the groundwaters were well-preserved during sampling due to the high pressure gradient from the borehole section to the tunnel. Included in this study are pristine and stagnant groundwater samples collected in 1991-2016 from 25 borehole sections at depths between 69 and 447 m.b.s.l (Table 2; Fig. A8). The groundwaters were analyzed for pH, $\delta^{18}\text{O}$, and concentrations of organic carbon (DOC), $\text{Fe(II)}_{\text{aq}}$, total Fe (Fe_{tot}), SO_4^{2-} , $\text{S(-II)}_{\text{aq}}$, Cl^- , K, Na, Mg, Ca, Si, and Sr. Samples were filtered through 0.45 μm membrane filters and collected in 100 mL plastic bottles, except for samples for $\text{S(-II)}_{\text{aq}}$ analysis that were collected unfiltered in 120 mL Winkler glass bottles, and for anions which were collected unfiltered in 250 mL plastic bottles (Drake et al., 2015b). The analytical methods and uncertainties have been reported elsewhere (Mathurin et al., 2014; Drake et al., 2015b). All data were retrieved from the SICADA database that is owned and quality-checked by SKB and only include samples with charge balances within $\pm 5\%$. The Cl^- concentrations and $\delta^{18}\text{O}$ values were used to trace the dominant origin of groundwater according to the method presented by Mathurin et al. (2012), that is, meteoric (Cl^- concentrations $< 1749 \text{ mg L}^{-1}$ and $\delta^{18}\text{O}$ values between -7.95‰ and -13‰), brackish marine (modelled as modern and past Baltic Sea water, with Cl^- concentrations $< 8000 \text{ mg L}^{-1}$ and $\delta^{18}\text{O}$ values between -4.7‰ and -7.95‰), saline (Cl^- concentrations $> 8000 \text{ mg L}^{-1}$) and thoroughly mixed (Cl^- concentrations between 1749 mg L^{-1} and 8000 mg L^{-1} , and $\delta^{18}\text{O}$ values between -8‰ and -13‰).

In November 2015, planktonic cells from both stagnant and pristine groundwater in the five borehole sections (Table 1) were collected on sterile polyvinylidene fluoride (PVDF), hydrophilic, 0.1 μm , 47 mm Durapore membrane filters (Merck Millipore). *In situ* conditions were maintained by connecting a High-Pressure Stainless Steel Filter Holder (Millipore) with

a downstream needle valve and pressure gauge directly to the borehole. After the filtration, the filter was aseptically placed in a sterile cryogenic tube (Thermo Scientific), which was immediately frozen in liquid nitrogen to allow transport to the laboratory without alterations in the cell numbers. Tubes were stored at -80°C until further processing. DNA was extracted using the PowerWater DNA isolation kit (MOBIO) by following the manufacturer's instructions except for the final elution where DNA was collected in $50\ \mu\text{L}$ of eluent. The quantity of the extracted DNA was analyzed with a Qubit 2.0 Fluorometer (Life Technologies). Extracted DNA was stored at $-20\ ^{\circ}\text{C}$ until further processing. 16S rRNA gene amplicon sequencing was carried out using published procedures (Wu et al., 2016). The UPARSE pipeline was used to process the sequences and cluster operational taxonomic units (OTUs) (Edgar, 2013). OTUs were then annotated against the SINA/SILVA database (SILVA 123, Quast et al. (2013)) and finally analyzed in Explicet 2.10.5 (Robertson et al., 2013). The amount of pair-end reads received from the sequencing facility, merged and quality trimmed reads, and amount of OTUs clustered can be found in Table A9. Final count values were normalized by relative abundance (i.e. % of total sample size). Phylogenetic trees were constructed in MEGA 7 (Kumar et al., 2016) after aligning sequences with MUSCLE (Edgar, 2004). 16S rRNA sequences are available at the NCBI database, accession number MF042363 - MF043058.

Iron isotope ratio ($^{56}\text{Fe}/^{54}\text{Fe}$, expressed as $\delta^{56}\text{Fe}$ relative to the IRMM-014 standard) was obtained for groundwaters, as follows: (i) pristine groundwaters from the 25 borehole sections (except B2) in November 2013 (number of observations (n) =24); and (ii) both pristine and stagnant groundwaters from borehole sections A2-A4 and B1-B2 in November 2015 (n =10). The Fe isotope ratio was determined using a Multi-Collector ICP-MS (Neptune, ThermoScientific, Germany) at ALS Laboratory Group, Luleå, Sweden. The instrumental settings and operating conditions are reported elsewhere (Van Heghe et al., 2012). The water

samples were evaporated to dryness and digested in a mixture of 5 mL HNO₃ (16 M) and 1 mL HCl (10 M) in a microwave oven for 1 h. The solution was then passed through an 0.8 mL anion exchange anion (Dowex 1-8, 50-100 mesh) for chemical purification of Fe, following the procedure of Malinovsky et al. (2003) and Ingri et al. (2006). According to Ingri et al. (2006), both the digestion method and anion-exchange purification procedure can give a near-quantitative recovery (> 95%) of the total Fe. To eliminate high concentrations of HCl, which were found to affect precise MC-ICPMS measurements of Fe, the Fe fractions after anion-exchange separation were transferred into Teflon beakers, evaporated on a hot plate to dryness and redissolved in 0.3 M HNO₃. The purified samples were diluted to 5.0 ± 0.5 mg L⁻¹ Fe with diluted HNO₃ and spiked with Ni at 5 mg L⁻¹. Nickel was used as an internal standard for instrumental fractionation of Fe isotopes. Standard deviation calculated from two independent consecutive measurements varied from 0.014-0.082‰. Both accuracy and long term-reproducibility (2 σ) assessed through analysis of in-house Fe isotope standard over a 15 years period are better than 0.06‰.

The speciation of Fe(II)_{aq} and S(-II)_{aq} in the groundwaters from the five borehole sections (A2-A4 and B1-B2) was predicted using the chemical equilibrium programme Visual MINTEQ (Gustafsson, 2013) (Table A10). The input parameters included temperature, pH, redox potential (Eh), Fe(II)_{aq}, S(-II)_{aq}, SO₄²⁻, K⁺, Na⁺, Mg²⁺, Ca²⁺, Si(H₄SiO₄), Sr²⁺, HCO₃⁻, Cl⁻, and DOC. Since Eh was not monitored for the five borehole sections, the value was taken from a borehole section at a corresponding depth in the study area where it was -175 mV (Nilsson et al., 2013; Gimeno et al., 2014). The temperature of the groundwaters fluctuated around +15 °C (Table 2). This value was taken for groundwaters for which temperature was not measured. The Stockholm humic model was used to simulate the formation of metal-DOM (dissolved organic matter) complexes (Gustafsson, 2001). It was assumed that the ratio of active DOM to DOC was 1.65 (Sjöstedt et al., 2010) and that 70% of the active DOM was

fulvic acid and the remaining 30% inactive with respect to proton and metal binding (Åström et al., 2010). $\text{Fe(II)}_{\text{aq}}$ and $\text{S(-II)}_{\text{aq}}$ was allowed to precipitate when the solubility product for mackinawite ($\log K_s$ of -3.6 at 25 °C) was exceeded.

4. RESULTS

4.1 Fe-isotopes of pyrite

The $\delta^{56}\text{Fe}$ values of fracture pyrite crystals were highly variable both within individual crystals and across the crystals and fractures, with no depth-related trend (Fig. 2a). Specifically, the values spanned in maximum from -1.50‰ to +2.76‰ and ranged by up to 2.70‰ within individual crystals and by 0.38‰-3.06‰ within single fractures (Fig. 2a,b; Table 3). A similar pattern was evident for the modern pyrite crystals where the values varied from -1.81‰ to +2.29‰ and ranged by up to 2.00‰ within individual crystals and by 1.65‰-3.52‰ within individual borehole sections (Figs. 2a,b and 3; Table 3). Most of fracture and modern pyrite crystals were euhedral with cubic habit and displayed very few overgrowths or zonations (Fig. 4a-f, A3-A6). There was no systematic difference in $\delta^{56}\text{Fe}$ between the rims and cores (Fig. A11) or between euhedral (mainly cubic) and subhedral crystals (Table 3, Fig. A12).

Both fracture and modern pyrite crystals displayed a similar unimodal distribution of $\delta^{56}\text{Fe}$ values, clustered around 0.1‰ and 0.3‰, respectively (Fig. 2b), which according to the Shapiro-Wilk test (Shapiro and Wilk, 1965) were not normally distributed. The result of a Mann-Whitney U test, which does not require the assumption of normality, showed that the isotopic compositions of these two populations of pyrite were statistically indistinguishable. When all the *in situ* determinations of $\delta^{56}\text{Fe}$ values for each crystal were averaged, the values for the pyrite crystals of these two populations exhibited a similar distribution pattern as observed for all the determinations (Fig. A13).

The pyrite crystals occurred alongside fine-grained FeS aggregates ($< 25 \mu\text{m}$) that were intergrown with calcites on all parts of the borehole instrumentation (Drake et al., 2015b) and to some extent had precipitated on the surface of magnetite (Fig. 4g) or partially to nearly completely replaced magnetite (Fig. 4h-l). Previous SEM-EDS investigations showed that the FeS precipitates exhibited molar S/Fe ratios of 0.91-1.09 (Drake et al., 2014), lying within the compositional range reported for mackinawite. However, these FeS aggregates were too fine-grained for SIMS analysis (attempts resulted in insufficient count rates).

4.2 Groundwater chemistry

The groundwater in the fracture network was chemically and isotopically diverse and modelled to be dominated by meteoric, brackish marine (modern and past Baltic Sea water), saline or be composed of a mixture of these waters (Figs. 2c and A8). The meteoric groundwater was mainly located in the upper 250 m, while the saline and brackish marine groundwaters reside at greater depths (Fig. A8).

In the pristine groundwaters, the concentrations of dissolved Fe_{tot} were stable over time (Table 2 and Fig. A8). However, the $\text{S(-II)}_{\text{aq}}$ concentrations were stable over time in sections A2 and A4, but varied up to three orders of magnitude in the other sections and had concentrations up to 3.70 mg L^{-1} (Table 2 and Fig. A8). The concentrations of dissolved Fe_{tot} and $\text{S(-II)}_{\text{aq}}$ showed no clear trend with depth (Fig. A8) and water type (Figs. 5a,b and A8). Due to the higher spatial-temporal variability in concentrations of $\text{S(-II)}_{\text{aq}}$, the molar ratio of $\text{S(-II)}_{\text{aq}}$ to $\text{Fe(II)}_{\text{aq}}$ varied in a manner similar to that of $\text{S(-II)}_{\text{aq}}$ (Table 2 and Fig. A8). The detectable and occasionally high concentrations of $\text{S(-II)}_{\text{aq}}$ as well as dissolved Fe_{tot} (Table 2 and Fig. A8) consisting entirely of $\text{Fe(II)}_{\text{aq}}$ (Drake et al., 2015b), provided evidence for stable reducing conditions in the system. This was further supported by strongly negative Eh values in other studied fractures at similar depths at the site (Nilsson et al., 2013; Gimeno et al.,

2014). The stagnant groundwater had similar Fe concentrations as the pristine groundwater but more variable and frequently substantially elevated $S(-II)_{aq}$ concentrations (Table 2). Visual MINTEQ modelling showed that, in addition to HS^- and H_2S , $FeHS^+$ is a major $S(-II)_{aq}$ species, accounting for 19-38% of the total dissolved $S(-II)_{aq}$ (Table A10). Accordingly, this species contributed significantly (24-47%) to the $Fe(II)_{aq}$ pools, in particular in the groundwaters with elevated $S(-II)_{aq}$ concentrations (high $S(-II)_{aq}$ to $Fe(II)_{aq}$ ratios) (Table A10).

4.3 Iron isotopic and microbial community composition in groundwaters

The $\delta^{56}Fe$ values of dissolved Fe_{tot} for all groundwater samples ($n=34$) varied from -1.75‰ to 0.39‰ (Fig. 2c,d, Table 3), with 10th-90th percentiles of -0.20‰ to 0.27‰ (Table 3). The $\delta^{56}Fe$ values were uncorrelated with depth, water type, pH, DOC/ Cl^- , $S(-II)_{aq}/Cl^-$, and Fe_{tot}/Cl^- (Figs. 2c and 5). In the borehole sections in which $\delta^{56}Fe$ was measured twice in pristine groundwater (2013 and 2015) and once in stagnant groundwater (2015), sections A3, A4, and B2 displayed almost identical $\delta^{56}Fe$ values both between and within sections, whereas sections A2 and B1 had one slightly more negative $\delta^{56}Fe$ value (Fig. 3).

The most abundant microbial phylogenetic groups in the groundwaters were Betaproteobacteria and Deltaproteobacteria followed by unclassified bacteria that collectively refer to sequences that did not match any “classified” phylum in the database (Figs. 6a and B1-10, Table A14). The abundance of these three groups differed greatly between the stagnant and pristine groundwaters (Fig. 6a, Table A14). In the stagnant groundwater in A2, the Nitrospirae phylum was also relatively high (20%). Microorganisms capable of utilizing S were abundant, with an overall dominance of S-oxidizing bacteria in borehole sections A2-4 and S-reducing bacteria in borehole sections B1-2 (except for B2-P) and considerable unsystematic differences between the stagnant and pristine groundwaters (Fig. 6b, Table A15).

The relative proportions of iron oxidizing bacteria and nitrate reducing bacteria were low, varying between 0.40-5.53% and 0.00-0.13%, respectively (Table A15). The stagnant groundwater in A2, A4 and B1 displayed a small but significant increase in the abundance of iron reducing bacteria (IRB) as compared to the pristine groundwater, while the percentage of nitrite oxidizing bacteria was strongly elevated in stagnant groundwater in A2 as to in the pristine groundwater (Fig. 6b, Table A15).

5. DISCUSSION

5.1 Iron isotope variability in groundwaters

Except for one strongly negative result (-1.75‰), the $\delta^{56}\text{Fe}$ values of dissolved Fe_{tot} in the groundwaters fell within the range of potential solid Fe sources in the fracture systems (Table 3). However, the $\delta^{56}\text{Fe}$ values of dissolved Fe_{tot} varied to a much smaller extent than the $\delta^{56}\text{Fe}$ values of fracture pyrite residing in fractures over a large depth span and modern pyrite from the same borehole section (Figs. 2a,c and 3). Also, the absence of a correlation between $\delta^{56}\text{Fe}$ with groundwater type and elevation (Fig. 2c) as well as major variables (Fig. 5) suggested that groundwater origin, depth, and composition had no significant influence on the isotope composition of dissolved Fe in the studied upper half kilometer of the fracture network. Thus, there is a high stability in the $\delta^{56}\text{Fe}$ values of dissolved Fe over both spatial and temporal dimensions. In consequence, the Fe isotopic composition of the dissolved Fe_{tot} , consisting entirely of $\text{Fe}(\text{II})_{\text{aq}}$ (Drake et al., 2015a,b), could not have had a significant influence on the much greater $\delta^{56}\text{Fe}$ variability in the coexisting pyrite.

Given the anoxic conditions of the groundwaters, an abundance of $\text{Fe}(\text{II})_{\text{aq}}$ and scarce occurrence of low-temperature Fe (hydr-)oxides in fractures at depths below 50 m (Drake et al., 2009; Dideriksen et al., 2010; Nilsson et al., 2013), iron-oxidizing bacteria identified in all

pristine and stagnant groundwaters in A2-4 and B1-2 (Fig. 6, Table A15) were most likely inactive or growing via an alternative electron donor. These features and data further suggested that the strongly (anomalously) negative $\delta^{56}\text{Fe}$ value in the groundwater at a depth of approximately 140 m.b.s.l (Fig. 2c) did not reflect a strong depletion of ^{56}Fe in a shrinking dissolved Fe(II) pool resulting from partial oxidation of the dissolved ferrous iron and formation of isotopically heavy Fe (hydr-)oxides (Bullen et al., 2001; Croal et al., 2004; Busigny et al., 2014). Instead, this anomalous value was most likely due to the activity of IRB, which were identified although in small numbers in the five borehole sections (Fig. 6b, Table A15), causing partial reductive dissolution of locally accumulated Fe(III)-bearing minerals which can produce a $\text{Fe(II)}_{\text{aq}}$ pool depleted in heavy Fe isotopes by approximately -2‰ (Beard, 1999; Brantley et al., 2004; Crosby et al., 2007; Johnson et al., 2008).

5.2 Evidence for low-temperature origin of modern and fracture pyrite

The temperature of groundwaters in the four borehole sections fluctuated less than 1.5 °C over the 17 years (14.3-15.6 °C, Table 2), which shows that no warm water (e.g., upflow of potential deep warmer fluids) has flowed through the boreholes during the formation of modern pyrite. The fracture pyrite is also expected to be formed under similar low-temperature conditions, because (i) fluid inclusions within co-genetic calcite crystals showed homogenization temperatures below 90 °C, commonly below 50 °C (Drake et al., 2015a, 2017); (ii) radiometric dating (Rb-Sr and U-Pb dating systems) suggested that the co-genetic calcite crystals were formed <400 Ma, during which no large hydrothermal systems have been active in this granitoid system (Drake et al., 2017); (iii) the fracture pyrite and co-genetic calcite displayed strong biogenic sulfur and carbon isotope signatures, suggesting extensive microbial activity and hence no high temperature fluids during the formation of the pyrite (Drake et al., 2013, 2015a); and (iv) thermochronological studies show that low-temperature

conditions prevailed the granitoid system from the Mesozoic until the present day (Guenther et al., 2017).

5.3 Modern pyrite

5.3.1 FeS and pyrite formation pathways

The stagnant groundwaters in the five borehole sections (A2-A4 and B1-B2) were oversaturated with respect to FeS (Drake et al., 2015b), consistent with abundant fine-grained FeS aggregates ($< 25 \mu\text{m}$) intergrown mainly with calcites on all parts of the borehole instrumentation (Drake et al., 2015b). These results provide evidence for the formation of FeS via direct reaction of $\text{Fe(II)}_{\text{aq}}$ and $\text{S(-II)}_{\text{aq}}$ speciated mainly as $\text{Fe}^{2+}/\text{FeHS}^-$ and $\text{HS}^-/\text{H}_2\text{S}$, respectively (Table A10), which are thermodynamically the most stable forms of dissolved Fe and sulfide under the reducing and alkaline conditions prevailing in the borehole sections (Rickard, 2006; Rickard et al., 2006; Rickard and Luther, 2007). It has been shown that Fe (hydr-)oxides (e.g. magnetite) are highly reactive towards dissolved sulfide (Canfield et al., 1992) and thus, can react with dissolved sulfide to form FeS. This process has contributed to the formation of FeS in the borehole sections, as evidenced by the partial to near-complete replacement of magnetite by FeS (Fig. 4). It was unlikely that magnetite formed during the withdrawal of the instrumentation and sampling campaigns, as those crystals are well-coated by FeS (Fig. 4).

The transformation of FeS precursor to pyrite has been suggested to (i) proceed mainly via the H_2S pathway in strictly anoxic environments where H_2S and HS^- are the dominant forms of dissolved sulfide (Rickard, 1997; Luther et al., 2003; Butler et al., 2004) and (ii) be dependent specifically on the concentrations of H_2S and polysulfides favoring the H_2S pathway and polysulfide pathway, respectively (Rickard and Luther, 2007). In turn, these two pathways favor pyrite formation via crystal growth and nucleation, respectively, which are

two distinct physical processes of formation of this mineral (Rickard and Luther, 2007). Considering the reducing and slightly alkaline conditions in the five borehole sections, $\text{H}_2\text{S}/\text{HS}^-$ are expected to be the dominant sulfide species in solution (Rickard and Luther, 2007) (Table A10). This favors transformation of FeS precursor to pyrite via the H_2S pathway, that is, the relatively slow process of crystal growth via the reaction of FeS and H_2S (Rickard and Luther III, 1997; Rickard and Luther, 2007). As suggested by Rickard et al. (1997) and Rickard and Luther III, (1997), the reaction involves the formation of an inner sphere complex between FeS (as electroactive cluster <5 nm in size) and H_2S followed by electron transfer between S(-II) and H(I) to produce S_2^{2-} with the rate-limiting step being the transport of electroactive FeS cluster to the site of pyrite growth. This pyrite-forming mechanism was further confirmed isotopically by Butler et al. (2004).

5.3.2 Depletion of ^{56}Fe in pyrite relative to the groundwater

Precipitates of FeS were observed more frequently than pyrite and occurred mainly as fine-grained but also partly as larger aggregates in the borehole sections (Drake et al., 2015b). Hence, during the lifetime of the borehole sections and thus the period of potential FeS formation (17 years), the pyritization was as a whole only partial. This partial pyritization can, when it occurs via crystal growth through the H_2S pathway as suggested for the pyrite here, cause systematically negative $\delta^{56}\text{Fe}$ values in the pyrite (down to $-2.2 \pm 0.7\%$) relative to the precursor phases (Guilbaud et al., 2011). Hence, pyrite formed from excess FeS can, via this kinetic isotopic fractionation, have played a significant role and largely controlled the formation of low $\delta^{56}\text{Fe}$ values in pyrite in the borehole sections (Fig. 2b,d; Fig. 3).

Another potential formation pathway of the low $\delta^{56}\text{Fe}$ values of pyrite is via reduction of magnetite that was found in several of the borehole sections (Fig. 4), and probably had formed as a result of activity of IRB that were identified (although in small numbers) in all sections

(Fig. 6b, Table A15). Previous experiments have shown that magnetite formed in relation to the activities of IRB and magnetotactic bacteria is depleted in isotopically heavy Fe by as much as 1.3‰ to 1.5‰ relative to the dissolved Fe (Johnson et al., 2005; Amor et al., 2016). In contrast, the Fe isotope fractionation during the partial reduction of Fe oxides by dissolved sulfide produces $\text{Fe(II)}_{\text{aq}}$ with values ranging from approximately 0.4‰ to -0.8‰ relative to the starting material (McAnena, 2011). Taken together, this causes the $\text{Fe(II)}_{\text{aq}}$ produced by partial sulfidization of magnetite (assuming this mineral has strongly negatively $\delta^{56}\text{Fe}$ values) to be isotopically lighter than the initial $\text{Fe(II)}_{\text{aq}}$. This means that FeS formed by sulfidization of magnetite in the borehole sections, a process clearly revealed by the SEM-EDS (Fig. 4), should have partly inherited the light Fe of magnetite and thus may have acted as an additional precursor for pyrite crystals with low $\delta^{56}\text{Fe}$ (Fig. 2b,d; Fig. 3).

5.3.3 Enrichment of ^{56}Fe in pyrite relative to the groundwater

Within the pyrite crystals, the frequently observed $\delta^{34}\text{S}$ increase from crystal center to rim (Fig. 7c) has been interpreted to reflect Rayleigh distillation processes (reservoir effects) caused by the development of closed-system conditions, that is, bacterial-sulfate-reduction rates exceed the supply rate of sulfate by advection and diffusion (Drake et al. 2015b). However, this reservoir effect acting on sulfate did not occur on the entire groundwater volume, but only in the micro-environment near the growing crystals (Drake et al. 2015b). A corresponding center-to-rim feature was not observed for the $\delta^{56}\text{Fe}$ values (Fig. 7b), except for in a very few crystals (highlighted in bold in Table A1). Hence, there was no correlation between $\delta^{56}\text{Fe}$ and $\delta^{34}\text{S}$ neither for the whole dataset of all pyrite crystals (Fig. 7a) nor the individual pyrite crystals typically with an overall increase in $\delta^{34}\text{S}$ values during growth (Fig. 7b,c). This is in contrast to several other studies of low-temperature pyrite for which $\delta^{56}\text{Fe}$ values co-vary positively with those of $\delta^{34}\text{S}$ (Archer and Vance, 2006, Lin et al. 2017). The

co-variation was interpreted to reflect progressive exhaustion of light S and Fe isotopes in the sulfate and reactive Fe pools, respectively, due to coupled microbial sulfate reduction and kinetic Fe isotope effects during the formation of Fe sulfides and partial pyritization (Archer and Vance, 2006, Lin et al. 2017). It is therefore unlikely that the groundwater near the growing pyrite crystals became progressively enriched in the heavy Fe isotope, in contrast to what has been found for sulfate (Drake et al. 2015b). As a consequence, a reservoir effect can not explain the large number of $^{56}\text{Fe}_{\text{pyrite}}$ observations higher or considerably higher than that of $\text{Fe(II)}_{\text{aq}}$ (Fig. 2b,d; Fig. 3).

The only experimentally demonstrated mechanism that can preferentially sequester $^{56}\text{Fe}_{\text{aq}}$ into FeS is presented by Wu et al. (2012) and occurs during FeS precipitation that reached isotopic equilibrium with $\text{Fe(II)}_{\text{aq}}$ in 38 days at pH=7, demonstrating that at neutral pH FeS particle coarsening is prohibited and Fe isotope exchange between the precipitated FeS and $\text{Fe(II)}_{\text{aq}}$ is quicker than in experiments at pH 4 conducted earlier by others (Butler et al., 2005; Guilbaud et al., 2011a). This mechanism is also possible for the FeS precipitates in the borehole sections, because they (i) formed at near-neutral pH and low temperatures (approximately +15 °C; Table 2), and (ii) are usually nanoparticles 1000 times smaller than pyrite (Rickard and Luther, 2007) and thus likely to have existed as nanosized particles in addition to the fine-grained aggregates observed by SEM-EDS (Drake et al., 2015b). In consequence, we suggest that FeS was resolubilized as ^{56}Fe -enriched electroactive FeS clusters that reacted with H_2S leading to formation of pyrite crystals that preserved the ^{56}Fe -enrichment of FeS, thus contributing to produce the pyrite $\delta^{56}\text{Fe}$ values within region 1 in Fig. 8. However, this mechanism requires nearly quantitative transformation of FeS to pyrite, as otherwise there is only partial pyritization that causes the pyrite to attain negative $\delta^{56}\text{Fe}$ values. We thus suggest that the process operates on very small scales, that is, the transformation of FeS to pyrite is (nearly) quantitative in certain micro-environments causing formed pyrite to

attain positive instead of negative $\delta^{56}\text{Fe}$ values. Furthermore, the occasionally very high $\text{S(-II)}_{\text{aq}}$ concentrations and molar ratios of $\text{S(-II)}_{\text{aq}}/\text{Fe(II)}_{\text{aq}}$ in the groundwaters (Table 2 and Fig. A8), and possibly even higher in micro-scale environments near the growing pyrite crystals due to high rates of microbial sulfate reduction (Drake et al., 2015b), increases the proportion of FeHS^+ (Table A10) and FeS_{aq} in solution (Wu et al., 2012). According to the experiment by Wu et al. (2012), the increase in the proportions of these species can further enhance the magnitude of the positive $\delta^{56}\text{Fe}$ value in FeS in equilibrium with $\text{Fe(II)}_{\text{aq}}$ by approximately 0.3‰, thus further increasing the $\delta^{56}\text{Fe}$ values in pyrite (region 2 in Fig. 8).

The pyrite crystals with highly positive $\delta^{56}\text{Fe}$ values, which cannot be directly explained by $\text{Fe(II)}_{\text{aq}}$ -FeS isotope equilibrium fractionation according to Wu et al. (2012) (region 3 in Fig. 8), mainly occurred in borehole sections A2 and B1 with comparatively higher isotope variability in dissolved Fe (Fig. 3). Except for one crystal with highly positive $\delta^{56}\text{Fe}$ values (1.86-2.29‰) in section B1 (Fig. 8, Table A1), the $\delta^{56}\text{Fe}$ values recorded in pyrite crystals in these two sections can be explained using the equilibrium Fe-isotope fractionation factors if the $\delta^{56}\text{Fe}$ value of dissolved Fe was approximately 0.25‰. Although 0.25‰ is higher than observed in the groundwater in these two sections (Fig. 3), it was within the range of dissolved Fe in the fracture system (90th percentile: 0.27‰, Table 3) and thus, could hypothetically have occasionally occurred in these two sections during the 17 years of pyrite formation. The highly positive $\delta^{56}\text{Fe}$ values recorded in one of the crystals in section B1 (1.86‰-2.29‰) would require a $\delta^{56}\text{Fe}$ value of dissolved Fe of approximately 1.00‰, which is much higher than observed in any of the groundwater samples (maximum 0.39‰) and thus, cannot be explained by equilibrium Fe-isotope fractionation between $\text{Fe(II)}_{\text{aq}}$ and FeS. The strongly positive $\delta^{56}\text{Fe}$ values in this particular crystal are intriguing because in other crystals in the same borehole section the $\delta^{56}\text{Fe}$ values were considerably lower (Fig. 8). This shows that even at small scales like a borehole section and over relatively short time periods (<17

years) a considerable spread in $\delta^{56}\text{Fe}$ values between individual pyrite crystals can develop. This may be related to the fact that multiple equilibrium and kinetic Fe-isotope fractionation processes may occur in parallel during the transfer of $\text{Fe(II)}_{\text{aq}}$ to FeS/pyrite causing the resulting FeS/FeS₂ to attain a broad range of $\delta^{56}\text{Fe}$ values.

5.4 Fracture pyrite

Although the fracture pyrite was of low-temperature origin as the modern pyrite, it was formed in a completely natural system (bedrock-fracture surfaces) over a large depth interval (Fig. 2a). In addition, the fracture pyrite is co-genetic with calcite with ages dating (microscale U-Pb geochronology) back from the Quaternary to mid-Mesozoicum (Drake et al., 2017), and thus represents a considerable span of ages. It is thus a noteworthy feature that the $\delta^{56}\text{Fe}$ values of the fracture pyrite were very similar to those of the modern pyrite both in terms of frequency-distribution patterns for the whole datasets (Fig. 2b), total ranges (Fig. 2a,b), intra-crystal variability (Fig. 7b,e; Table A1, A2), and absence of correlation with the $\delta^{34}\text{S}$ values (Fig. 7). This indicates that the mechanisms underlying $\delta^{56}\text{Fe}$ patterns in pyrite in low-temperature granitoid-fracture settings are fundamental and in general independent of variables such as depth, age, introduced artificial materials, groundwater chemistry, and S-isotope systematics. Hence, the mechanisms presented here for the modern pyrite can in general be applied to pyrite formed in fracture systems in the continental crust over large time scales.

6. CONCLUSIONS

This study investigated the inter- and intra-crystal variability of $\delta^{56}\text{Fe}$ in low-temperature pyrite crystals sampled from instrumentation in five borehole sections and from fracture systems in the upper 1 km of fractured bedrock on the Baltic Shield. The main findings were:

- The $\delta^{56}\text{Fe}$ values of the modern pyrite crystals (< 17 years old) in the five borehole sections (-1.81‰ to +2.29‰) varied to a much greater extent than those of the groundwaters in the same sections (-0.48‰ to +0.13‰), providing strong *in situ* evidence for a large Fe isotope fractionation during the conversion of $\text{Fe(II)}_{\text{aq}}$ to FeS and ultimately to pyrite in anoxic systems.
- Although a variety of abiotic and biotic processes can produce $\text{Fe(II)}_{\text{aq}}$ with highly fractionated Fe isotopes ultimately recorded in pyrite, the results of this study demonstrated that the fractionation processes during the capture of $\text{Fe(II)}_{\text{aq}}$ by pyrite alone (i.e. the formation of FeS and subsequent pyritization) can produce a large range of $\delta^{56}\text{Fe}$ values for low-temperature pyrite crystals. A considerable part of the $\delta^{56}\text{Fe}$ variability in pyrite can be explained by applying equilibrium Fe-isotopic fractionation factors between $\text{Fe(II)}_{\text{aq}}$ and FeS reported in the literature (Wu et al., 2012). Such an equilibrium is favored by the internal conditions within the fractures and borehole sections (slightly alkaline pH and relatively low temperatures), the morphological features of the FeS (aggregates identified and nanosized particles likely to occur), and the slow formation rate of pyrite via the H_2S pathway in the systems. This equilibrium predicts that FeS has systematically higher $\delta^{56}\text{Fe}$ values than the coexisting groundwaters and thus, can be resolubilized and reacted with dissolved sulfide, contributing to the enrichment of heavy Fe isotopes seen in a considerable part of the pyrite crystals.
- Strongly negative $\delta^{56}\text{Fe}$ values in pyrite that cannot be explained by equilibrium $\text{Fe(II)}_{\text{aq}}$ -FeS isotope fractionation were probably caused by two mechanisms: kinetic isotopic fractionation during partial transformation of micro-sized FeS to pyrite and sulfidization of magnetite.

- The $\delta^{56}\text{Fe}$ values did not correlate with those of $\delta^{34}\text{S}$ either in the entire set of all pyrite crystals or across individual pyrite crystals. The absence of such covariation is interpreted as due to the fact that unlike S whose fractionation is strongly linked to microbially mediated production of sulfide, multiple equilibrium and kinetic Fe-isotope fractionation processes could occur in parallel during the transfer of $\text{Fe(II)}_{\text{aq}}$ to FeS/pyrite causing the resulting FeS/FeS_2 to attain a broad range of $\delta^{56}\text{Fe}$ values.
- The almost identical Fe-isotope patterns for the modern pyrites, formed on artificial materials (borehole instrumentation) within the relatively short operational period of the borehole (17 years), and the pyrites formed throughout the low-temperature evolution of the fracture network (Mesozoic-Quaternary), show that the mechanisms presented here for the modern pyrite are fundamental and generally valid for formation of low-temperature pyrite in bedrock fractures.

ACKNOWLEDGEMENTS

We gratefully acknowledge the Swedish Nuclear Fuel and Waste Management Co. (SKB) and Nova Centre for University Studies Research & Development for giving access to the drill cores, the Äspö HRL, and the SICADA database. Swedish research council (contract 2017-05186 to H.D. and 2014-4398 to M.D.) and Formas (contract 2017-00766 to H.D. and M.W.) are thanked for financial support. Linda Alakangas (SKB) and Tobias Berger (Linnaeus University) are thanked for carrying out part of the water sampling while Frédéric Mathurin (Linnaeus University) is thanked for selecting the borehole sections from which groundwaters were sampled for Fe isotope analysis and for insightful discussions on water origin/mixing in the fracture network. We also thank Lev Ilyinsky and Kerstin Lindén at NordSIM for assistance during SIMS analyses. This is Nordsim contribution number 588.

FIGURE CAPTIONS

Fig. 1. (a) Location and (b) layout (sub-horizontal view) of Laxemar and the Äspö Hard Rock Laboratory (Äspö HRL), SE Sweden. The location and orientation of the sampled boreholes A and B (KA3105A and KA3385A), main tunnel, spiral tunnels, and elevator shaft are indicated. Layout of boreholes B and A are shown in (c) and (d), along with (e) equipment and precipitate details (“black sulfide precipitates” include FeS, pyrite, and chalcopyrite). Borehole A continues for 68.95 m while borehole B (not shown in detail) ends where the section 1 terminates at 34.18 m. The figure was modified from Drake et al. (2015b).

Fig. 2 Summary of Fe isotope ratio ($\delta^{56}\text{Fe}$) in groundwaters from the Äspö HRL and fracture and modern pyrites (*in situ* SIMS analyses). (a) Depth distribution of $\delta^{56}\text{Fe}$ values in fracture and modern pyrite crystals; the values of individual crystals are connected by a line; (b) histogram of $\delta^{56}\text{Fe}$ values in fracture and modern pyrite crystals; (c) depth distribution of $\delta^{56}\text{Fe}$ values in pristine and stagnant groundwaters from the Äspö HRL with water types defined according to the groundwater classification by Mathurin et al. (2012); data points represent the mean ± 1 standard deviation of duplicate determinations; (d) histogram of $\delta^{56}\text{Fe}$ values in pristine and stagnant groundwaters from the Äspö HRL.

Fig. 3 Comparison of $\delta^{56}\text{Fe}$ values in pyrite crystals and groundwaters in the borehole sections where data for both materials were collected (A2, A3, A4, B1, and B2).

Fig. 4 Back-scattered SEM images of selected modern pyrite crystals from borehole sections A3 (a=A3_crystal 3), B2 (b=B2_crystal 12), B1 (c=B1_crystal 13) and A2 (d=A2_crystal 10);

fracture pyrite crystals (e=KLX07A:356_crystal 2 and f=KSH01:239_crystal 2); and FeS (bright) aggregates intergrown with magnetite (dark) in borehole sections A2 (g), A3 (h-j), and A4 (k-l). Transects analyzed for both $\delta^{56}\text{Fe}$ (the value for each spot was reported in parentheses) and $\delta^{34}\text{S}$ were indicated in the pyrite crystals. The identification of magnetite was supported by its elemental composition determined by EDS analysis and its appearance observed by reflective light microscope. The images of (a-f) were reproduced from Drake et al. (2013, 2015b).

Fig. 5 $\delta^{56}\text{Fe}$ values versus (a) the concentration ratios of total dissolved Fe (Fe_{tot}) to Cl^- ; (b) the concentration ratios of dissolved S^{2-} to Cl^- ; (c) the concentration ratios of dissolved organic carbon (DOC) to Cl^- ; and (d) pH for all pristine groundwaters. The water type was defined using the groundwater classification of Mathurin et al. (2012).

Fig. 6 Bacterial communities in stagnant (S) and pristine (P) groundwaters collected from five borehole sections (A2, A3, A4, B1, and B2) at the Äspö HRL. Sequences were clustered into operational taxonomic units (OTUs) at the 0.97 similarity level. (a) Heatmap representing the relative abundance of the OTUs grouped into phyla. The Proteobacteria phylum was further subdivided into α -, β -, γ -, and δ -Proteobacteria classes. The rest of the OTUs that do not belong to any “classified” phylum were grouped and represented as “Unclassified”. (b) Stacked bar graph showing the OTUs that were previously clustered into bacterial groups described for their ability to use different compounds. Bacterial sequences that were not relevant for this study were grouped as “Others”. The rest of the sequences that do not belong to any “classified” phylum were represented as “Unclassified”.

Fig. 7 Relationships between $\delta^{34}\text{S}$ and $\delta^{56}\text{Fe}$ values for modern and fracture pyrite. (a) $\delta^{34}\text{S}$ versus $\delta^{56}\text{Fe}$ for all modern pyrite crystals; (b) intra-crystal variation of $\delta^{56}\text{Fe}$ values in selected modern pyrite crystals with an increase in $\delta^{34}\text{S}$ values from crystal centers to rims as shown in (c), the analytical transects in these crystals were shown in Fig. 4a-d; (d) $\delta^{34}\text{S}$ versus $\delta^{56}\text{Fe}$ values for all fracture pyrite crystals; (e) intra-crystal variation of $\delta^{56}\text{Fe}$ values in selected fracture pyrite crystals with a increase in $\delta^{34}\text{S}$ values from crystal centres to rims as shown in (f), the analytical transects of KLX07A:356_2 and KSH01:239_2 were shown in Fig. 4e and f. The data of $\delta^{34}\text{S}$ values were reproduced from Drake et al. (2013, 2015a,b).

Fig. 8 Comparison of $\delta^{56}\text{Fe}$ values in pyrite crystals and groundwaters from the same borehole section. For sections A2 and B1 in which the groundwaters had large Fe-isotopic variations (Fig. 2), the $\delta^{56}\text{Fe}$ values in pyrite crystals were plotted against the values of all three groundwater samples. The values of individual crystals are connected by a line. The fields between the solid lines (Region 1) and dashed lines (Region 2) were modelled using equilibrium Fe-isotope fractionation factors of $0.32\pm 0.29\text{‰}$ and $0.64\pm 0.36\text{‰}$, respectively, predicted by Wu et al. (2012) based on experiments at pH=7, including FeS precipitation via mixing $\text{Fe(II)}_{\text{aq}}$ solution and sulfide solution at a 10:1 Fe:S ratio, and Fe isotope exchange between isotopically “normal” $\text{Fe(II)}_{\text{aq}}$ and ^{56}Fe -enriched FeS with addition of free sulfide.

References

- Amor, M., Busigny, V., Louvat, P., Gélabert, A., Cartigny, P., Durand-Dubief, M., Ona-Nguema, G., Alphandéry, E., Chebbi, I. and Guyot, F., 2016. Mass-dependent and-independent signature of Fe isotopes in magnetotactic bacteria. *Science*, 352(6286): 705-708.

- Archer, C., Vance, D., 2006. Coupled Fe and S isotope evidence for Archean microbial Fe(III) and sulfate reduction. *Geology*, 34(3): 153-156.
- Ask, H., Morosini, M., Tiberg, L., 2005. Oskarshamn Site Investigation: Drilling of Cored Borehole KLX03. SKB Report P-05-167. SKB, Stockholm, Sweden.
- Åström, M.E., Nystrand, M., Gustafsson, J.P., Österholm, P., Nordmyr, L., Reynolds, J.K. and Peltola, P., 2010. Lanthanoid behaviour in an acidic landscape. *Geochimica et Cosmochimica Acta*, 74(3): 829-845.
- Balci, N., Bullen, T.D., Witte-Lien, K., Shanks, W.C., Motelica, M. and Mandernack, K.W. , 2006. Iron isotope fractionation during microbially stimulated Fe(II) oxidation and Fe(III) precipitation. *Geochimica et Cosmochimica Acta*, 70(3): 622-639.
- Beard, B.L., 1999. Iron Isotope Biosignatures. *Science*, 285(5435): 1889-1892.
- Berner, R.A., 1967. Thermodynamic stability of sedimentary iron sulfides. *American Journal of Science*, 265(9): 773-785.
- Boetius, A., Ravenschlag, K., Schubert, C.J., Rickert, D., Widdel, F., Gieseke, A., Amann, R., Jørgensen, B.B., Witte, U. and Pfannkuche, O., 2000. A marine microbial consortium apparently mediating anaerobic oxidation of methane. *Nature*, 407(6804): 623-626.
- Brantley, S.L., Liermann, L.J., Guynn, R.L., Anbar, A., Icopini, G.A. and Barling, J., 2004. Fe isotopic fractionation during mineral dissolution with and without bacteria. *Geochimica et Cosmochimica Acta*, 68(15): 3189-3204.
- Bullen, T.D., White, A.F., Childs, C.W., Vivit, D.V., Schulz, M., 2001. Demonstration of significant abiotic iron isotope fractionation in nature. *Geology*, 29(8): 699.
- Busigny, V., Planavsky, N.J., Jézéquel, D., Crowe, S., Louvat, P., Moureau, J., Viollier, E. and Lyons, T.W., 2014. Iron isotopes in an Archean ocean analogue. *Geochimica et Cosmochimica Acta*, 133: 443-462.

- Butler, I.B., Archer, C., Vance, D., Oldroyd, A., Rickard, D., 2005. Fe isotope fractionation on FeS formation in ambient aqueous solution. *Earth and Planetary Science Letters*, 236(1-2): 430-442.
- Butler, I.B., Böttcher, M.E., Rickard, D., Oldroyd, A., 2004. Sulfur isotope partitioning during experimental formation of pyrite via the polysulfide and hydrogen sulfide pathways: implications for the interpretation of sedimentary and hydrothermal pyrite isotope records. *Earth and Planetary Science Letters*, 228(3-4): 495-509.
- Canfield, D.E., 2001. Isotope fractionation by natural populations of sulfate-reducing bacteria. *Geochimica et Cosmochimica Acta*, 65: 1117-1124.
- Canfield, D.E., Raiswell, R., Bottrell, S.H., 1992. The reactivity of sedimentary iron minerals towards sulfide. *American Journal of Science*, 292(9): 659-683.
- Chapman, J.B., Weiss, D.J., Shan, Y., Lemburger, M., 2009. Iron isotope fractionation during leaching of granite and basalt by hydrochloric and oxalic acids. *Geochimica et Cosmochimica Acta*, 73(5): 1312-1324.
- Croal, L.R., Johnson, C.M., Beard, B.L., Newman, D.K., 2004. Iron isotope fractionation by Fe(II)-oxidizing photoautotrophic bacteria. *Geochimica et Cosmochimica Acta*, 68(6): 1227-1242.
- Crosby, H.A., Roden, E.E., Johnson, C.M., Beard, B.L., 2007. The mechanisms of iron isotope fractionation produced during dissimilatory Fe(III) reduction by *Shewanella putrefaciens* and *Geobacter sulfurreducens*. *Geobiology*, 5(2): 169-189.
- Detmers, J., Bruchert, V., Habicht, K.S., Kuever, J., 2001. Diversity of sulfur isotope fractionations by sulfate-reducing prokaryotes. *Applied and Environmental Microbiology*, 67(2): 888-94.
- Dideriksen, K., Christiansen, B.C., Frandsen, C., Balic-Zunic, T., Mørup, S. and Stipp, S.L.S., 2010. Paleo-redox boundaries in fractured granite. *Geochimica et Cosmochimica Acta*, 74(10): 2866-2880.

- Drake, H., Åström, M.E., Heim, C., Broman, C., Astrom, J., Whitehouse, M., Ivarsson, M., Siljestrom, S. and Sjoval, P., 2015a. Extreme ^{13}C depletion of carbonates formed during oxidation of biogenic methane in fractured granite. *Nature Communications*, 6: 7020.
- Drake, H., Åström, M.E., Tullborg, E.-L., Whitehouse, M., Fallick, A.E., 2013. Variability of sulphur isotope ratios in pyrite and dissolved sulphate in granitoid fractures down to 1km depth – Evidence for widespread activity of sulphur reducing bacteria. *Geochimica et Cosmochimica Acta*, 102: 143-161.
- Drake H., Hallbeck L., Pedersen K., Rosdahl A., Tullborg E.-L., Wallin B., Sandberg B. and Blomfeldt T. (2014) Investigation of Sulphide Production in Core-drilled Boreholes in Äspö Hard Rock Laboratory. Boreholes KA3110A, KA3385A and KA3105A. Swedish Nuclear Fuel and Waste Management Co. (SKB), Stockholm, Sweden, Report TR-13-12.
- Drake, H., Heim, C., Roberts, N.M.W., Zack, T., Tillberg, M., Broman, C., Ivarsson, M., Whitehouse, M.J. and Åström, M.E., 2017. Isotopic evidence for microbial production and consumption of methane in the upper continental crust throughout the Phanerozoic eon. *Earth and Planetary Science Letters* 470, 108-118.
- Drake, H., Tullborg, E.-L., MacKenzie, A.B., 2009. Detecting the near-surface redox front in crystalline bedrock using fracture mineral distribution, geochemistry and U-series disequilibrium. *Applied Geochemistry*, 24(5): 1023-1039.
- Drake, H., Tullborg, E.-L., Whitehouse, M., Sandberg, B., Blomfeldt, T. and Åström, M.E., 2015b. Extreme fractionation and micro-scale variation of sulphur isotopes during bacterial sulphate reduction in deep groundwater systems. *Geochimica et Cosmochimica Acta*, 161: 1-18.
- Edgar, R.C., 2004. MUSCLE: multiple sequence alignment with high accuracy and high throughput. *Nucleic acids research*, 32(5): 1792-1797.
- Edgar, R.C., 2013. UPARSE: highly accurate OTU sequences from microbial amplicon reads. *Nature methods*, 10(10): 996-998.

- Fabre, S., Nédélec, A., Poitrasson, F., Strauss, H., Thomazo, C. and Nogueira, A., 2011. Iron and sulphur isotopes from the Carajás mining province (Pará, Brazil): Implications for the oxidation of the ocean and the atmosphere across the Archaean–Proterozoic transition. *Chemical Geology*, 289(1-2): 124-139.
- Gimeno, M.J., Auqué, L.F., Acero, P., Gómez, J.B., 2014. Hydrogeochemical characterisation and modelling of groundwaters in a potential geological repository for spent nuclear fuel in crystalline rocks (Laxemar, Sweden). *Applied Geochemistry*, 45: 50-71.
- Guenther, W.R., Reiners, P.W., Drake, H., Tillberg, M., 2017. Zircon, titanite, and apatite (U - Th)/He ages and age - eU correlations from the Fennoscandian Shield, southern Sweden. *Tectonics*, 36(7): 1254-1274.
- Guilbaud, R., Butler, I.B., Ellam, R.M., Rickard, D., Oldroyd, A., 2011a. Experimental determination of the equilibrium Fe isotope fractionation between and FeSm (mackinawite) at 25 and 2°C. *Geochimica et Cosmochimica Acta*, 75(10): 2721-2734.
- Guilbaud, R., Butler, I.B., Ellam, R.M., 2011b. Abiotic pyrite formation produces a large Fe isotope fractionation. *Science*, 332(6037): 1548-51.
- Guilbaud, R., Butler, I.B., Ellam, R.M., Rickard, D., 2010. Fe isotope exchange between Fe(II)aq and nanoparticulate mackinawite (FeSm) during nanoparticle growth. *Earth and Planetary Science Letters*, 300(1-2): 174-183.
- Gustafsson, J., 2013. Visual MINTEQ ver. 3.1. Department of Land and Water Resources Engineering, KTH (Royal Institute of Technology), SE-100 44, Stockholm, Sweden. www2.lwr.kth.se/English/OurSoftware/vminteq/index.htm.
- Gustafsson, J.P., 2001. Modeling the acid–base properties and metal complexation of humic substances with the Stockholm Humic Model. *Journal of Colloid and Interface Science*, 244(1): 102-112.
- Hinrichs, K.U., Hayes, J.M., Sylva, S.P., Brewer, P.G., DeLong, E.F., 1999. Methane-consuming archaeobacteria in marine sediments. *Nature*, 398(6730): 802-5.

- Icopini, G., Anbar, A., Ruebush, S., Tien, M., Brantley, S., 2004. Iron isotope fractionation during microbial reduction of iron: the importance of adsorption. *Geology*, 32(3): 205-208.
- Ingri, J., Malinovsky, D., Rodushkin, I., Baxter, D.C., Widerlund, A., Andersson, P., Gustafsson, Ö., Forsling, W. and Öhlander, B., 2006. Iron isotope fractionation in river colloidal matter. *Earth and Planetary Science Letters*, 245(3): 792-798.
- Johnson, C.M., Beard, B.L., Roden, E.E., 2008. The iron isotope fingerprints of redox and biogeochemical cycling in modern and ancient earth. *Annual Review of Earth and Planetary Sciences*, 36(1): 457-493.
- Johnson, C.M., Roden, E.E., Welch, S.A., Beard, B.L., 2005. Experimental constraints on Fe isotope fractionation during magnetite and Fe carbonate formation coupled to dissimilatory hydrous ferric oxide reduction. *Geochimica et Cosmochimica Acta*, 69(4): 963-993.
- Kiczka, M., Wiederhold, J.G., Frommer, J., Kraemer, S.M., Bourdon, B. and Kretzschmar, R., 2010. Iron isotope fractionation during proton- and ligand-promoted dissolution of primary phyllosilicates. *Geochimica et Cosmochimica Acta*, 74(11): 3112-3128.
- Kumar, S., Stecher, G., Tamura, K., 2016. MEGA7: Molecular Evolutionary Genetics Analysis version 7.0 for bigger datasets. *Molecular Biology and Evolution*.
- Leavitt, W.D., Halevy, I., Bradley, A.S., Johnston, D.T., 2013. Influence of sulfate reduction rates on the Phanerozoic sulfur isotope record. *Proceedings of the National Academy of Sciences*, 110: 11244–11249.
- Lin, Z., Sun, X., Lu, Y., Strauss, H., Xu, L., Gong, J., Teichert, B.M.A., Lu, R., Lu, H., Sun, W. and Peckmann, J., 2017. The enrichment of heavy iron isotopes in authigenic pyrite as a possible indicator of sulfate-driven anaerobic oxidation of methane: Insights from the South China Sea. *Chemical Geology*, 449: 15-29.
- Lin, Z., Sun, X., Peckmann, J., Lu, Y., Xu, L., Strauss, H., Zhou, H., Gong, J., Lu, H. and Teichert, B.M.A., 2016. How sulfate-driven anaerobic oxidation of methane affects the sulfur isotopic composition of pyrite: A SIMS study from the South China Sea. *Chemical Geology*, 440: 26-41.

- Luther, G., Taillefert, M., Rozan, T., Rickard, D., 2003. Geochemical implications of the polysulfide vs sulfide pyrite formation reactions based on real time measurements of soluble reactants, ABSTRACTS OF PAPERS OF THE AMERICAN CHEMICAL SOCIETY. AMER CHEMICAL SOC 1155 16TH ST, NW, WASHINGTON, DC 20036 USA, pp. U912-U912.
- Malinovsky, D., Stenberg, A., Rodushkin, I., Andren, H., Ingri, J., Öhlander, B. and Baxter, D.C., 2003. Performance of high resolution MC-ICP-MS for Fe isotope ratio measurements in sedimentary geological materials. *Journal of Analytical Atomic Spectrometry*, 18(7): 687-695.
- Marin-Carbonne, J., Rollion-Bard, C., Bekker, A., Rouxel, O., Agangi, A., Cavalazzi, B., Wohlgemuth-Ueberwasser, C.C., Hofmann, A. and McKeegan, K.D., 2014. Coupled Fe and S isotope variations in pyrite nodules from Archean shale. *Earth and Planetary Science Letters*, 392: 67-79.
- Mathurin, F.A., Åström, M.E., Drake, H., Maskenskaya, O.M., Kalinowski, B.E., 2014. REE and Y in groundwater in the upper 1.2km of Proterozoic granitoids (Eastern Sweden) – Assessing the role of composition and origin of groundwaters, geochemistry of fractures, and organic/inorganic aqueous complexation. *Geochimica et Cosmochimica Acta*, 144: 342-378.
- Mathurin, F.A., Astrom, M.E., Laaksoharju, M., Kalinowski, B.E., Tullborg, E.L., 2012. Effect of tunnel excavation on source and mixing of groundwater in a coastal granitoidic fracture network. *Environmental Science & Technology*, 46(23): 12779-86.
- McAnena, A., 2011. The reactivity and isotopic fractionation of Fe-bearing minerals during sulfidation: an experimental approach (doctoral dissertation). Page 1-244. Newcastle University . Retrieved from. <http://hdl.handle.net/10443/1212>.
- Mikutta, C., Wiederhold, J.G., Cirpka, O.A., Hofstetter, T.B., Bourdon, B. and Gunten, U.V., 2009. Iron isotope fractionation and atom exchange during sorption of ferrous iron to mineral surfaces. *Geochimica et Cosmochimica Acta*, 73(7): 1795-1812.
- Munier, R., 2004. Statistical analysis of fracture data, adapted for modelling Discrete Fracture Networks-Version 2. SKB.

- Nilsson, A.-C., Gimeno, M.J., Tullborg, E.-L., Mathurin, F., John, S., 2013. Hydrogeochemical Data Report. Site Descriptive Modelling Äspö SDM. Swedish nuclear Fuel and Waste Management Co. (SKB). Stockholm, Sweden: R-13-26.
- Quast, C., Pruesse, E., Yilmaz, P., Gerken, J., Schweer, T., Yarza, P., Peplies, J. and Glöckner, F.O., 2013. The SILVA ribosomal RNA gene database project: improved data processing and web-based tools. *Nucleic acids research*, 41(D1): D590-D596.
- Rickard, D., 1997. Kinetics of pyrite formation by the H₂S oxidation of iron (II) monosulfide in aqueous solutions between 25 and 125 C: The rate equation. *Geochimica et Cosmochimica Acta*, 61(1): 115-134.
- Rickard, D., 2006. The solubility of FeS. *Geochimica et Cosmochimica Acta*, 70(23): 5779-5789.
- Rickard, D., Griffith, A., Oldroyd, A., Butler, I., Lopezcapel, E., Manning, D. and Apperley, D., 2006. The composition of nanoparticulate mackinawite, tetragonal iron(II) monosulfide. *Chemical Geology*, 235(3-4): 286-298.
- Rickard, D., Luther, G.W., 2007. Chemistry of Iron Sulfides. *Chemical reviews*, 107(2): 514-562.
- Rickard, D., Luther III, G.W., 1997. Kinetics of pyrite formation by the H₂S oxidation of iron (II) monosulfide in aqueous solutions between 25 and 125°C: the mechanism. *Geochimica et Cosmochimica Acta*, 61(1): 135-147.
- Ries, J.B., Fike, D.A., Pratt, L.M., Lyons, T.W., Grotzinger, J.P., 2009. Superheavy pyrite ($^{34}\text{S}_{\text{pyr}} > ^{34}\text{S}_{\text{CAS}}$) in the terminal Proterozoic Nama Group, southern Namibia: A consequence of low seawater sulfate at the dawn of animal life. *Geology*, 37(8): 743-746.
- Robertson, C.E., Harris, J.K., Wagner, B.D., Granger, D., Browne, K., Tatem, B., Feazel, L.M., Park, K., Pace, N.R. and Frank, D.N., 2013. Explicet: graphical user interface software for metadata-driven management, analysis and visualization of microbiome data. *Bioinformatics*, 29: 3100-3101.
- Rouxel, O.J., Bekker, A., Edwards, K.J., 2005. Iron isotope constraints on the Archean and Paleoproterozoic ocean redox state. *Science*, 307(5712): 1088-91.

- Schoonen, M., Barnes, H., 1991. Reactions forming pyrite and marcasite from solution: I. Nucleation of FeS₂ below 100°C. *Geochimica et Cosmochimica Acta*, 55(6): 1495-1504.
- Shapiro, S., Wilk, M., 1965. An analysis of variance test for normality. *Biometrika*, 52(3): 591-611.
- Sjöstedt, C.S., Gustafsson, J.P., Köhler, S.J., 2010. Chemical equilibrium modeling of organic acids, pH, aluminum, and iron in Swedish surface waters. *Environmental Science & Technology*, 44(22): 8587-8593.
- Van Heghe, L., Engström, E., Rodushkin, I., Cloquet, C., Vanhaecke, F., 2012. Isotopic analysis of the metabolically relevant transition metals Cu, Fe and Zn in human blood from vegetarians and omnivores using multi-collector ICP-mass spectrometry. *Journal of Analytical Atomic Spectrometry*, 27(8): 1327-1334.
- Virtasalo, J.J., Laitala, J.J., Lahtinen, R., Whitehouse, M.J., 2015. Pyritic event beds and sulfidized Fe (oxyhydr)oxide aggregates in metalliferous black mudstones of the Paleoproterozoic Talvivaara formation, Finland. *Earth and Planetary Science Letters*, 432: 449-460.
- Virtasalo, J.J., Whitehouse, M.J., Kotilainen, A.T., 2013. Iron isotope heterogeneity in pyrite fillings of Holocene worm burrows. *Geology*, 41(1): 39-42.
- Wahlgren, C.-H., Curtis, P., Hermanson, J., Forssberg, O., Oehman, J., Fox, A., La Pointe, P., Drake, H., Triumph, C.-A. and Mattsson, H., 2008. *Geology Laxemar. Site descriptive modelling SDM-Site Laxemar*, Swedish Nuclear Fuel and Waste Management Co.
- Whitehouse, M.J., Fedo, C.M., 2007. Microscale heterogeneity of Fe isotopes in > 3.71 Ga banded iron formation from the Isua Greenstone Belt, southwest Greenland. *Geology*, 35(8): 719-722.
- Wu, L., Druschel, G., Findlay, A., Beard, B.L., Johnson, C.M., 2012. Experimental determination of iron isotope fractionations among Fe²⁺_{aq}-FeS_{aq}-Mackinawite at low temperatures: Implications for the rock record. *Geochimica et Cosmochimica Acta*, 89: 46-61.
- Wu, X., Holmfeldt, K., Hubalek, V., Lundin, D., Åström, M., Bertilsson, S. and Dopson, M., 2016. Microbial metagenomes from three aquifers in the Fennoscandian shield terrestrial deep biosphere reveal metabolic partitioning among populations. *ISME J*, 10(5): 1192-203.

Yoshiya, K., Sawaki, Y., Hirata, T., Maruyama, S., Komiya, T., 2015. In-situ iron isotope analysis of pyrites in ~3.7Ga sedimentary protoliths from the Isua supracrustal belt, southern West Greenland. *Chemical Geology*, 401: 126-139.

Zhang, F., Zhu, X., Yan, B., Kendall, B., Peng, X., Li, J., Algeo, T.J. and Romaniello, S.,2015. Oxygenation of a Cryogenian ocean (Nanhua Basin, South China) revealed by pyrite Fe isotope compositions. *Earth and Planetary Science Letters*, 429: 11-19.

ACCEPTED MANUSCRIPT

Table 1 Summary of borehole sections in which both pyrite and groundwater were sampled.

Borehole Section	Abbreviation	Distance from tunnel wall (m)	Section volume (L)	Depth (m b.s.l.)	Borehole length (m)
KA3015A: section 2	A2	25.51–52.01	65.2	415	68.95
KA3015A: section 3	A3	22.51–24.51	4.90	415	68.95
KA3015A: section 4	A4	17.01–19.51	6.20	415	68.95
KA3385A: section 1	B1	32.05–34.18	4.50	445	34.18
KA3385A: section 2	B2	6.05–31.05	61.5	445	34.18

Table 2. Iron isotope and hydrochemical data of pristine and stagnant groundwaters from the five borehole sections (A2-A4 and B1-2) at the Äspö HRL.

Borehole section	Water sampled	Sampling date	$\delta^{56}\text{Fe}$	Temp °C	pH	Cl ⁻ mg L ⁻¹	$\delta^{18}\text{O}$	Fe(II) _{aq} mg L ⁻¹	Fe _{tot} mg L ⁻¹	S(-II) _{aq} mg L ⁻¹	SO ₄ ²⁻ mg L ⁻¹	DOC mg L ⁻¹	HCO ₃ ⁻ mg L ⁻¹	Na mg L ⁻¹	K mg L ⁻¹	Ca mg L ⁻¹	Mg mg L ⁻¹	Si mg L ⁻¹	Sr mg L ⁻¹	S(-II) _{aq} /Fe(II) _{aq}
A2	Pristine	2012-02-06	-	-	7.67	2672	-10.0	-	0.24	0.19	251.6	5.0	-	1230	7.45	608	42.3	7.17	11.0	-
	Pristine	2012-02-14	-	-	-	-	-10.1	-	0.17	-	-	5.1	-	1130	6.32	612	43.2	7.73	10.1	-
	Pristine	2013-10-31	-0.087	14.8	7.58	2503	-9.15	0.16	0.16	0.11	227.2	5.9	146.7	1290	6.55	439	42.3	7.04	8.34	1.23
	Pristine	2014-04-08	-	14.6	7.61	2519	-10.2	0.16	0.17	0.11	245.0	5.9	136.7	1150	6.72	480	43.4	7.61	9.43	1.18
	Pristine	2014-12-03	-	14.6	7.61	2531	-	-	0.16	0.11	244.2	-	126.2	1210	6.44	489	40.5	7.18	8.52	-
	Stagnant	2015-05-04	-	-	-	2464	-10.2	-	-	5.13	212.2	-	-	1160	5.88	455	35.3	5.66	-	-
	Pristine	2015-05-05	-	-	-	2565	-9.87	0.16	0.17	0.11	246.6	-	-	1210	6.33	502	40.1	6.58	-	1.20
	Stagnant	2015-11-09	-0.478	-	-	2471	-9.39	0.06	0.07	3.49	226.6	-	-	1230	8.06	440	49.3	6.60	-	102
	Pristine	2015-11-10	-0.048	-	-	2521	-9.32	0.21	0.21	0.09	242.1	-	-	1240	7.76	462	48.8	7.23	-	0.75
	Pristine	2016-05-18	-	-	-	2548	-9.19	0.20	0.20	0.11	244.5	-	-	1230	6.98	476	47.9	6.91	-	0.96
A3	Pristine	1995-03-10	-	-	7.60	3520	-8.70	0.30	0.36	-	217.0	3.1	125	1260	8.00	754	101	6.20	11.0	-
	Pristine	2011-10-11	-	14.3	7.63	2382	-8.63	0.18	0.21	0.26	223.0	6.1	206.1	1070	7.52	404	62.7	7.68	6.57	2.49
	Pristine	2012-02-06	-	-	7.73	2613	-9.40	-	0.41	0.23	225.0	6.0	-	1150	8.00	494	52.4	7.73	8.92	-
	Pristine	2012-02-14	-	-	-	-	-9.00	-	0.26	-	-	7.3	-	-	-	-	-	-	-	-
	Pristine	2013-05-20	-	14.6	7.59	2368	-8.75	0.28	0.28	0.27	211.2	7.0	228.2	1090	11.0	366	76.5	7.39	6.17	1.67
	Pristine	2013-10-31	0.078	14.7	7.55	2277	-8.39	0.27	0.27	0.17	219.9	7.2	221	1260	9.93	302	76.7	6.55	5.47	1.08
	Pristine	2014-04-07	-	14.6	7.52	2366	-9.58	0.28	0.29	0.16	216.6	6.8	200.9	1150	11.0	344	85.1	6.87	6.18	0.99
	Pristine	2014-11-06	-	15.0	7.56	2510	-8.14	0.30	0.30	0.12	256.9	6.2	190.3	1300	10.9	391	85.4	6.61	6.24	0.72
	Stagnant	2015-04-27	-	-	-	2446	-9.19	-	-	1.07	239.4	-	-	1240	11.2	356	80.1	5.81	-	-
	Pristine	2015-04-27	-	-	-	2457	-9.33	0.30	0.31	0.23	247.2	-	-	1260	11.2	362	80.9	5.92	-	1.30
Stagnant	2015-11-09	0.045	-	-	2562	-8.72	0.29	0.29	0.19	252.8	-	-	1290	12.4	393	80.9	6.43	-	1.15	
Pristine	2015-11-09	0.060	-	-	2549	-8.72	0.30	0.30	0.14	254.2	-	-	1280	12.3	396	80.2	6.39	-	0.82	
Pristine	2016-05-10	-	-	-	2476	-8.64	0.28	0.29	0.15	244.9	-	-	1270	10.5	390	76.0	6.14	-	0.91	

A4	Pristine	2011-10-10	-	14.6	7.56	1684	-8.65	0.29	0.33	0.13	217.3	6.4	217.3	1070	9.21	365	71.1	7.60	5.74	0.77
	Pristine	2012-02-06	-	-	7.62	2341	-9.20	-	0.28	0.40	222.8	6.8	-	1090	10.6	390	66.7	7.31	6.67	-
	Pristine	2013-05-20	-	14.3	7.53	2349	-8.72	0.48	0.48	0.11	222.1	7.2	231.0	1110	14.4	342	85.7	7.29	5.50	0.41
	Pristine	2013-10-30	0.077	15.4	7.52	2306	-8.28	0.41	0.41	0.12	219.8	7.4	221.6	1260	12.7	281	86.1	6.44	4.82	0.50
	Pristine	2014-04-03	-	15.0	7.53	2376	-9.31	0.44	0.45	0.11	226.2	6.7	202.9	1150	13.6	329	91.5	6.78	5.77	0.45
	Pristine	2014-04-08	-	14.6	7.53	2400	-9.03	0.44	0.44	0.13	228.6	6.8	203.3	1170	13.6	331	91.9	6.84	5.83	0.52
	Pristine	2014-11-06	-	14.8	7.54	2477	-8.31	0.44	0.44	0.12	255.9	6.3	187.9	1280	12.9	363	89.9	6.40	5.60	0.49
	Stagnant	2015-05-05	-	-	-	2485	-9.15	-	-	0.80	237.0	-	-	1260	12.7	347	84.4	5.70	-	-
	Pristine	2015-05-05	-	-	-	2452	-9.15	0.42	0.42	0.10	243.2	5.7	-	1230	12.5	347	81.9	5.83	-	0.42
	Stagnant	2015-11-09	-	-	-	2548	-8.64	0.41	0.41	0.14	253.4	5.2	-	1290	13.4	387	84.6	6.30	-	0.60
	Pristine	2015-11-09	0.026	-	-	2548	-8.69	0.42	0.42	0.13	251.7	5.5	-	1280	13.2	383	83.3	6.24	-	0.54
	Pristine	2016-05-18	0.126	-	-	2532	-8.84	0.40	0.40	0.11	249.6	5.5	-	1260	11.6	393	76.7	6.00	-	0.48
B1	Pristine	1995-01-11	-	-	7.70	6650	-10.4	0.15	0.15	-	443.0	0.9	10.0	2080	8.50	1861	60.5	5.10	30.9	-
	Pristine	1995-03-10	-	-	7.50	6710	-10.5	0.13	0.15	-	450.0	1.1	10.0	2090	8.40	1860	63.1	5.00	29.7	-
	Pristine	1998-03-02	-	-	7.80	6630	-10.1	0.16	0.16	-	428.0	1.2	11.8	2180	9.00	1820	67.6	3.70	30.8	-
	Pristine	1998-09-28	-	-	7.80	6690	-10.1	0.19	0.24	0.04	-	1.2	11.8	2150	8.81	1800	61.6	4.40	24.1	0.35
	Pristine	1999-09-29	-	-	7.90	7010	-10.5	0.16	0.16	0.03	403.0	1.0	10.0	2350	9.60	1974	66.1	5.20	29.2	0.31
	Pristine	2000-04-10	-	-	7.80	6900	-10.3	0.17	0.17	0.01	411.0	1.3	10.9	2200	10.3	1890	64.9	4.26	31.2	0.06
	Pristine	2001-09-28	-	-	7.70	6670	-12.5	0.21	0.21	-	375.0	0.8	12.0	2220	10.7	1850	70.9	4.93	32.1	0.00
	Pristine	2002-09-24	-	-	7.75	6819	-10.9	0.18	0.19	0.01	394.3	1.0	10.9	2170	11.0	1920	65.4	4.70	33.6	0.06
	Pristine	2003-09-15	-	-	7.24	7040	-11.2	0.19	0.20	-	402.0	1.0	10.5	2230	10.6	2030	64.5	4.58	34.4	-
	Pristine	2005-10-07	-	-	7.52	6590	-10.7	0.21	0.21	0.02	378.0	1.2	24.9	2000	8.94	1780	72.0	6.15	31.0	0.13
	Pristine	2006-10-16	-	-	7.55	6240	-10.5	0.21	0.22	0.13	370.0	1.3	23.7	1850	10.2	1690	66.8	6.27	32.6	1.05
	Pristine	2007-10-10	-	-	7.58	6390	-10.7	0.21	0.21	0.16	378.0	1.2	25.8	2190	9.94	1840	68.1	6.07	33.5	1.33
	Pristine	2008-09-29	-	-	7.54	6780	-10.9	0.19	0.21	0.10	379.0	3.6	21.7	2130	11.1	1890	70.5	6.42	36.4	0.92
	Pristine	2009-09-21	-	-	7.48	7040	-10.2	0.22	0.23	0.07	378.0	1.4	21.6	2210	10.2	2020	66.5	6.43	34.0	0.58
	Stagnant	2010-03-30	-	-	7.58	6490	-	0.21	0.22	0.04	368.0	37.8	25.7	2230	10.4	1890	65.1	6.60	35.9	0.34
	Stagnant	2010-03-30	-	-	7.55	7560	-	0.19	0.21	0.02	417.0	4.7	19.6	2410	11.0	2270	61.6	6.25	43.3	0.21
	Stagnant	2010-04-21	-	-	7.52	6770	-	0.22	0.23	0.02	384.0	15.6	26.4	2090	9.57	1850	65.2	6.66	33.6	0.12
	Stagnant	2010-06-01	-	-	7.49	7100	-	0.25	0.26	0.17	374.0	28.1	21.7	2010	9.5	2030	63.6	6.3	34.6	1.19

	Stagnant	2010-06-15	-	-	7.46	6990	-	0.28	0.29	2.81	378.0	222	25.0	2080	10.1	2110	66.9	6.31	36.0	17.38
	Pristine	2011-01-20	-	-	7.54	6759	-10.8	0.27	0.29	0.16	357.5	14.5	28.6	2260	10.3	2010	69.6	6.39	36.0	1.06
	Pristine	2011-05-24	-	15.6	7.49	6369	-10.5	0.22	0.22	0.04	374.8	1.5	29.4	1980	9.33	1680	73.2	6.53	31.3	0.33
	Pristine	2011-11-15	-	14.6	7.50	6327	-10.5	0.21	0.21	0.05	367.9	1.5	29.8	2000	10.3	1730	65.5	6.36	31.5	0.42
	Pristine	2012-05-07	-	14.5	7.48	6331	-10.8	0.22	0.22	-	364.1	1.4	28.4	2100	9.56	1800	66.7	6.36	33.4	-
	Pristine	2012-11-14	-	-	7.55	7051	-	0.22	0.22	0.02	369.5	1.1	17.3	-	-	-	-	-	-	0.16
	Pristine	2012-11-14	-	-	7.52	1892	-	0.20	0.20	-	345.9	1.2	26.3	-	-	-	-	-	-	-
	Pristine	2012-11-22	-	14.8	7.50	6649	-11.1	0.20	0.20	-	352.8	1.4	27.3	2280	10.6	1950	69.1	6.35	35.2	-
	Pristine	2013-05-06	-	14.5	7.52	6853	-11.2	0.20	0.20	-	373.6	1.4	25.6	2120	10.7	1940	64.2	6.14	34.0	-
	Pristine	2013-11-13	0.058	14.8	7.51	7077	-11.4	0.19	0.20	0.02	385.7	1.3	25.1	2330	10.4	2020	68.6	5.49	35.2	0.18
	Pristine	2014-05-14	-	14.7	7.49	7179	-11.9	0.20	0.20	0.05	380.6	1.3	25.4	2430	11.5	2040	69.0	4.44	41.2	0.44
	Stagnant	2014-11-28	-	-	-	-	-	-	0.37	-	-	-	-	2560	10.6	2410	59.6	5.11	43.4	-
	Pristine	2014-11-28	-	14.6	7.50	7266	-10.8	0.19	0.19	0.02	391.9	1.4	24.4	2400	10.2	2160	62.8	5.29	38.7	0.19
	Pristine	2015-05-26	-	-	-	7314	-11.4	0.20	0.21	-0.02	406.2	-	-	2450	10.9	2130	61.9	5.45	-	-
	Pristine	2015-11-05	-0.428	-	-	7502	-11.1	0.19	0.19	-0.02	388.8	-	-	2520	10.8	2540	61.9	5.53	-	-
	Stagnant	2015-11-11	-0.145	-	-	8240	-11.3	0.17	0.17	0.05	422.2	-	-	2680	11.0	2820	57.8	5.26	-	0.52
	Pristine	2016-05-09	-	-	-	7489	-10.8	0.19	0.19	-0.02	407.0	-	-	2520	10.1	2290	58.2	5.09	-	-
B2	Pristine	1999-04-06	-	-	8.20	6930	-10.1	0.16	0.16	0.12	428.0	2.8	10.7	2160	7.9	1855	65.9	3.80	21.5	1.31
	Pristine	2005-10-07	-	-	7.29	6330	-10.7	0.21	0.21	-	376.0	1.3	24.9	2010	8.66	1790	72.4	6.21	31.4	-
	Stagnant	2010-05-11	-	-	7.63	7500	-	0.20	0.23	0.13	406.0	5.7	20.9	2300	10.5	2230	65.3	6.40	40.8	1.13
	Pristine	2012-11-14	-	-	7.47	7293	-	0.17	0.19	0.37	369.3	-	23.3	-	-	-	-	-	-	3.81
	Pristine	2012-11-15	-	-	7.67	7116	-	0.20	0.21	-	356.2	-	19.3	-	-	-	-	-	-	-
	Stagnant	2015-11-10	0.016	-	-	8125	-11.4	0.17	0.17	0.04	428.7	-	-	2730	11.3	2890	58.8	5.29	-	0.41
	Pristine	2015-11-11	0.041	-	-	8127	-11.3	0.17	0.17	0.02	430.5	-	-	2760	11.2	2880	58.2	5.24	-	0.21
	Pristine	2016-05-10	-	-	-	8073	-10.9	0.17	0.17	-0.02	434.5	-	-	2690	10.6	2560	54.6	4.82	-	-

-No data

Table 3 Iron isotopic composition of groundwaters and solid materials in the studied fracture system.

			Number of observations	Minimum (‰)	10 th percentile (‰)	Median (‰)	90 th percentile (‰)	Maximum (‰)
Pyrite ^a	Modern pyrite	All data	227	-1.81	-0.60	0.23	0.92	2.29
		Variation in individual crystal	46	0.00	0.12	0.44	1.15	2.00
	Fracture pyrite	Euhedral (cubic) crystals	146	-1.63	-0.55	0.19	0.63	1.71
		Subhedral crystals	81	-1.81	-0.89	0.35	1.19	2.80
		All data	494	-1.50	-0.78	0.11	1.30	2.76
		Variation in individual crystal	106	0.04	0.12	0.57	1.49	2.70
		Euhedral (cubic) crystals	59	-1.21	-0.38	0.17	1.30	2.76
	Subhedral crystals	51	-1.50	-0.99	0.05	1.28	2.76	
Groundwater ^a	All data		34	-1.75	-0.20	0.08	0.27	0.39
	Pristine groundwaters from sections A2-A4 and B1-B2 in 2013		4	-0.09	-0.04	0.07	0.08	0.08
	Pristine groundwaters from sections A2-A4 and B1-B2 in 2015		5	-0.43	-0.28	0.03	0.05	0.06
	Stagnant groundwaters from sections A2-A4 and B1-B2 in 2015		5	-0.48	-0.35	0.02	0.09	0.13
Fe sources ^b	Fe silicates		5	-0.57	-0.56	-0.43	-0.36	-0.35
	Amorphous Fe hydroxides		8	-0.97	-0.38	-0.38	0.08	0.23
	Low-temperature goethite, magnetite and hematite		15	-0.35	-0.25	0.10	0.69	1.14

^aThis study^bDideriksen et al. (2010)

Highlights:

- Dissolved Fe in the upper 500 m of fractured crystalline bedrock has stable $\delta^{56}\text{Fe}$ over both spatial and temporal dimensions
- Strong field evidence for a large Fe isotope fractionation during the conversion of $\text{Fe}(\text{II})_{\text{aq}}$ to FeS and eventually to pyrite
- The interplay of various Fe-isotope fractionation processes can hinder the development of Fe-S isotope co-variation in pyrite

ACCEPTED MANUSCRIPT

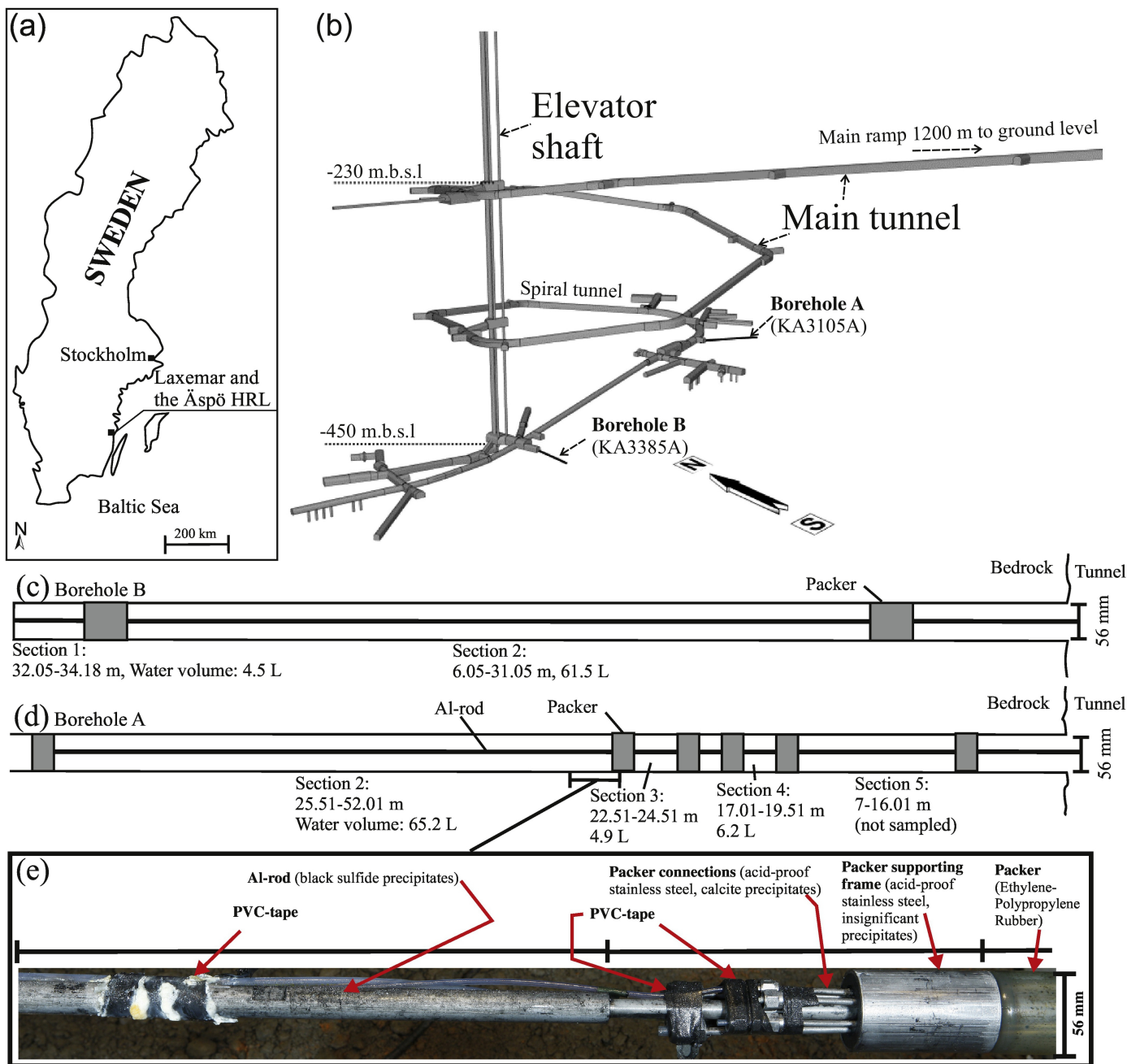


Figure 1

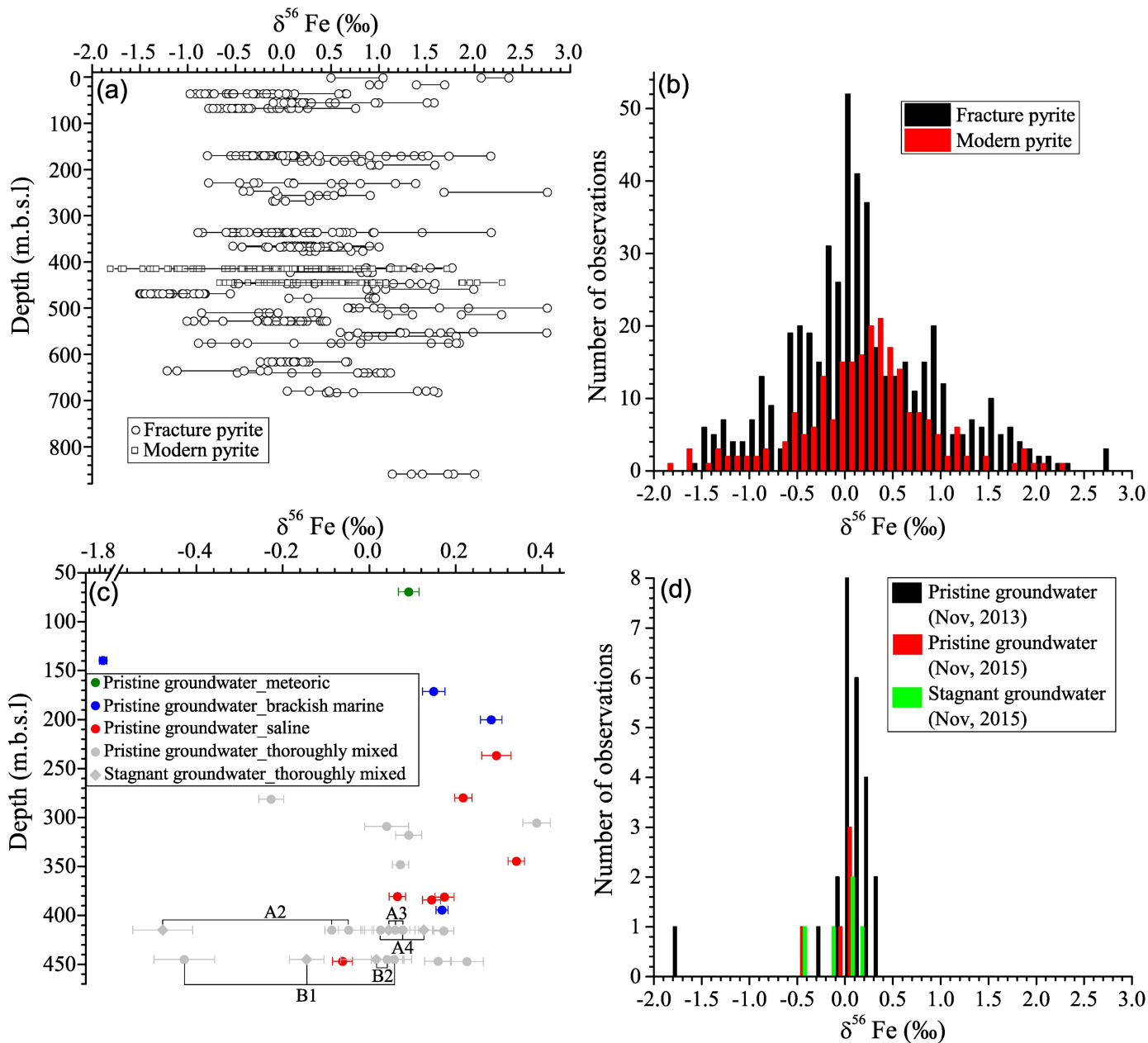


Figure 2

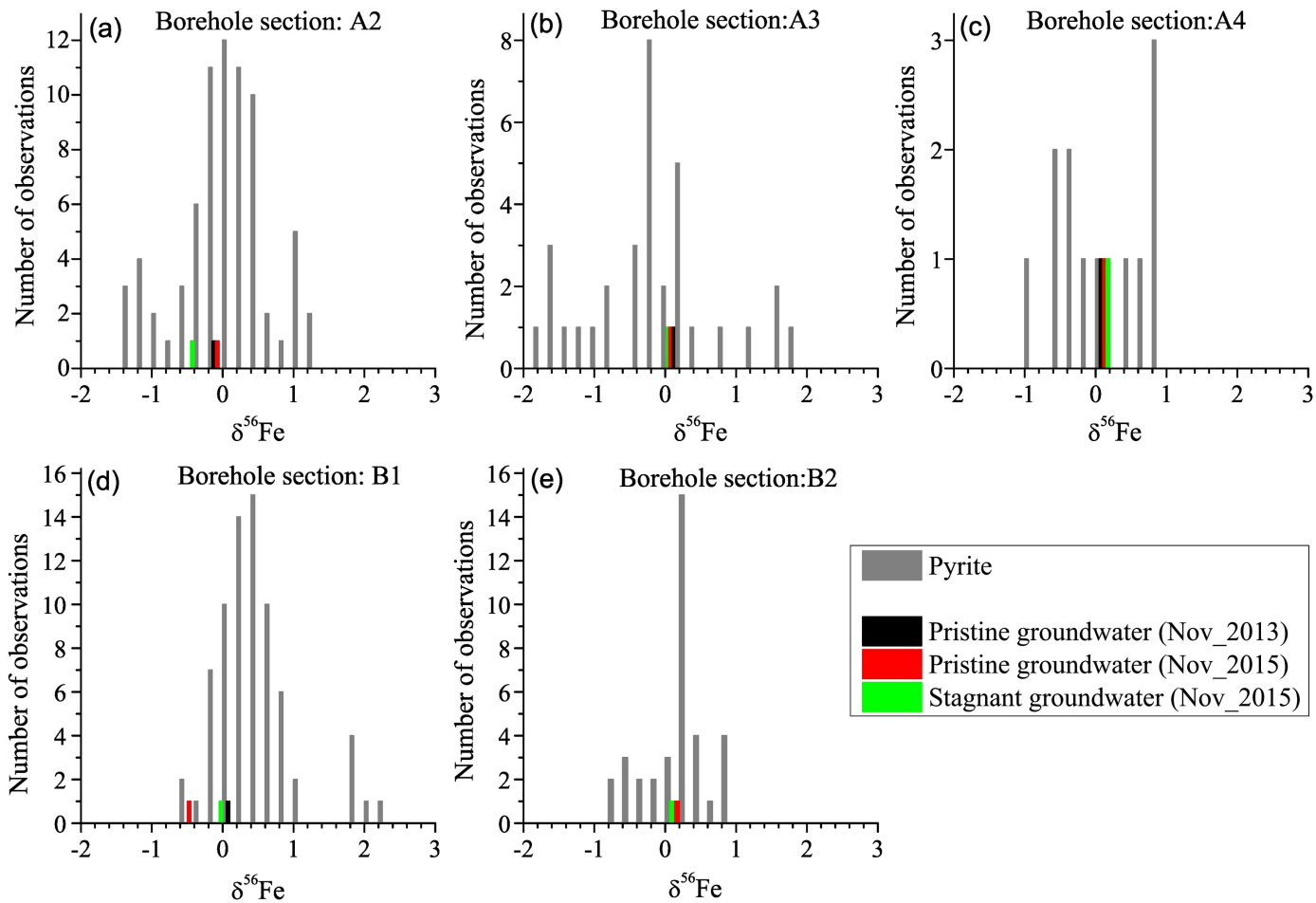


Figure 3

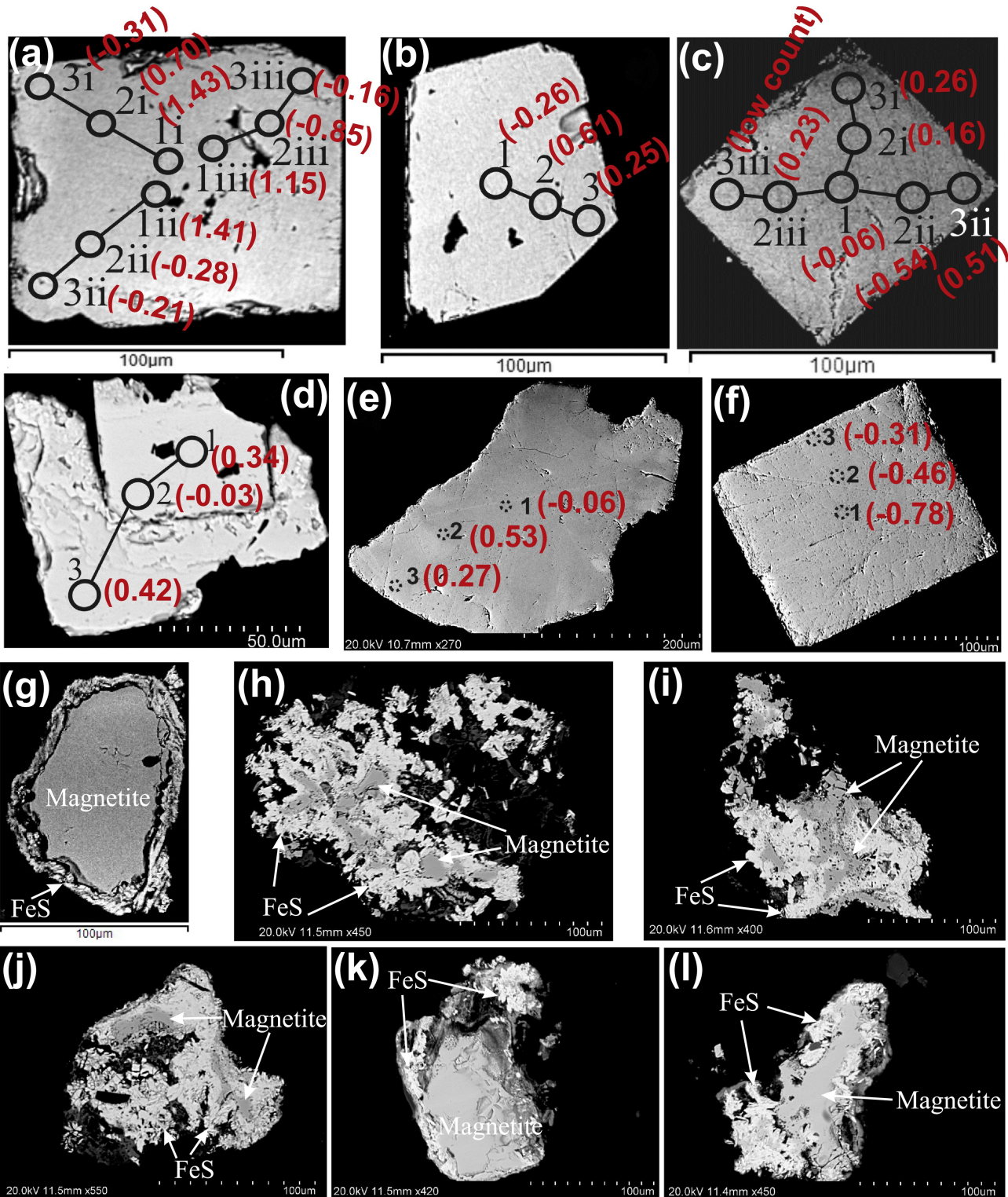


Figure 4

Groundwater type ● Meteoric ● Thoroughly mixed
 ● Brackish marine ● Saline

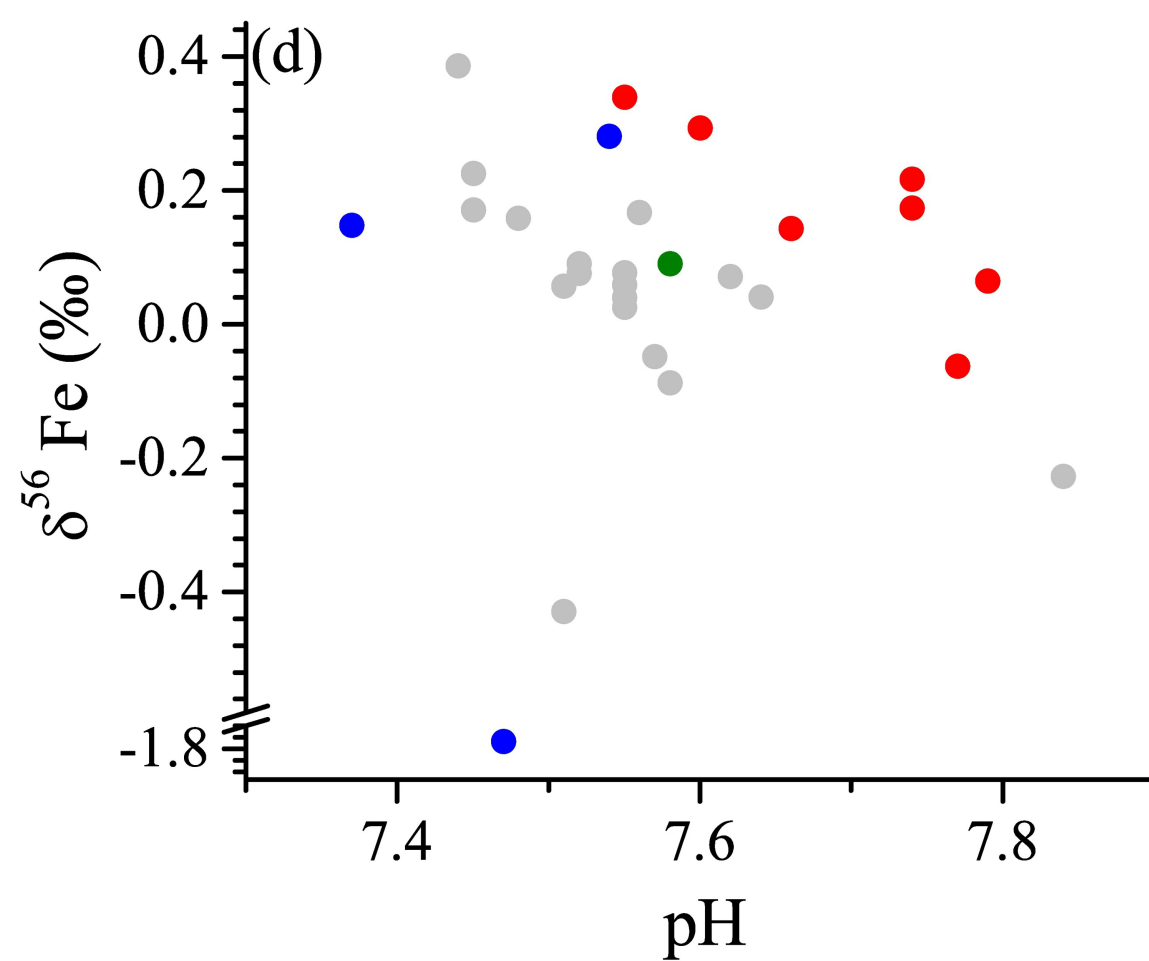
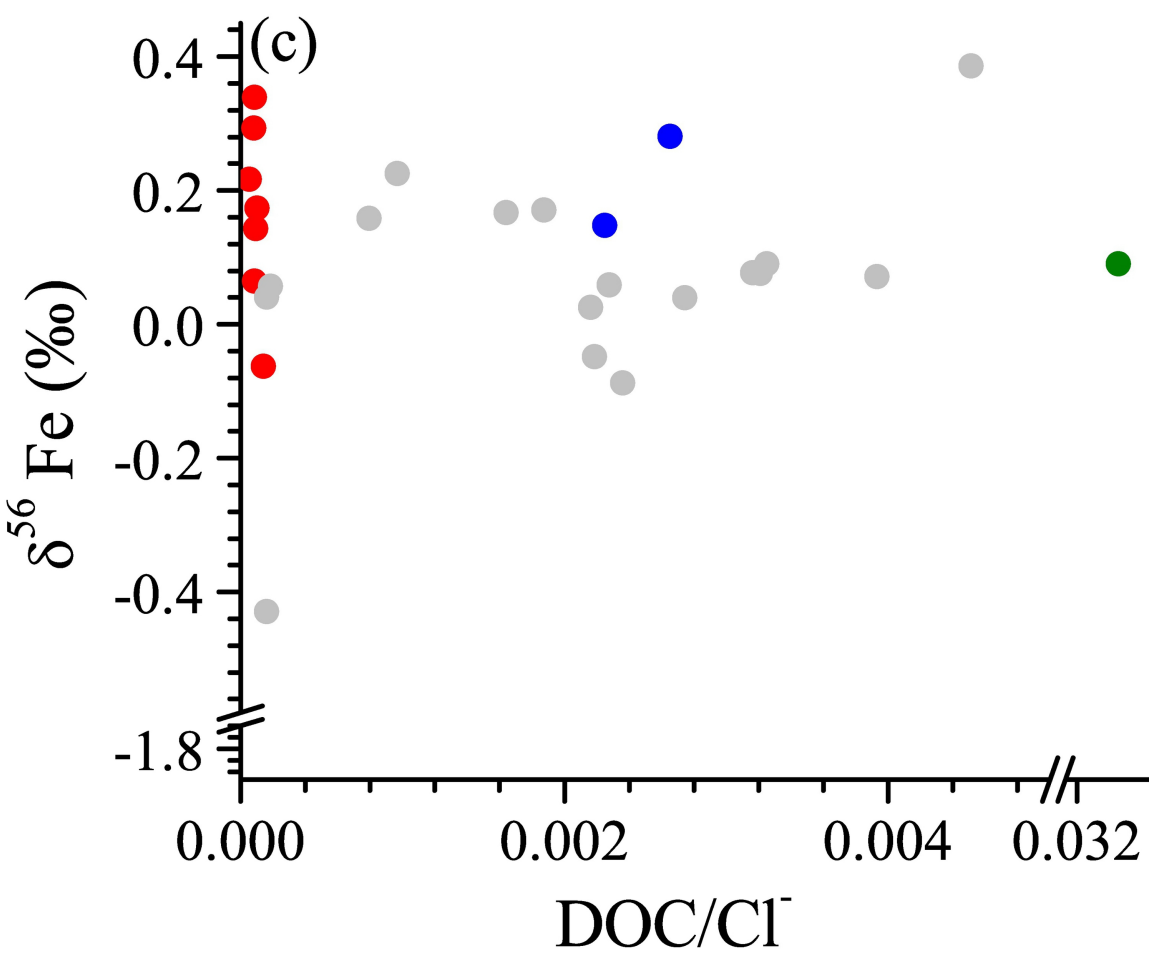
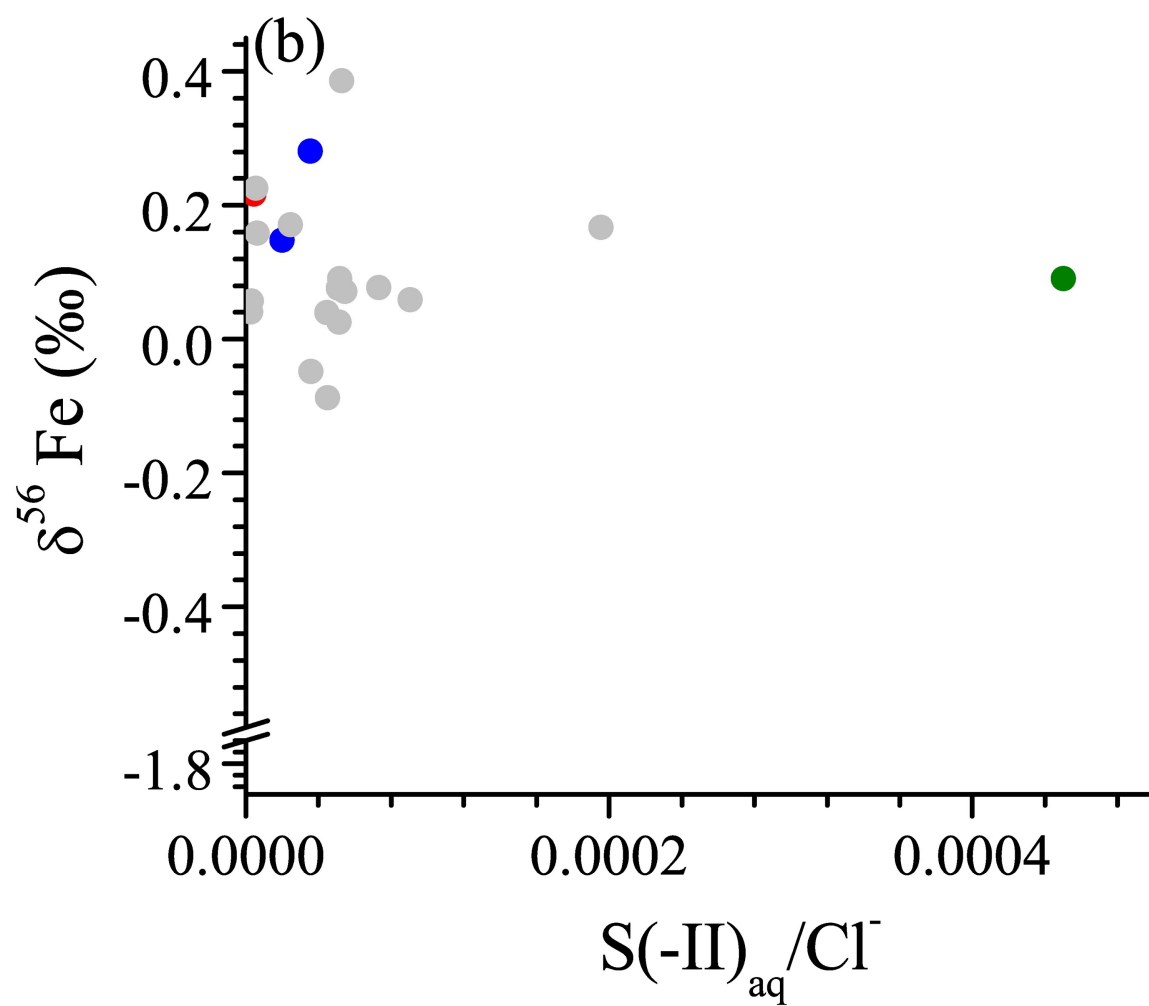
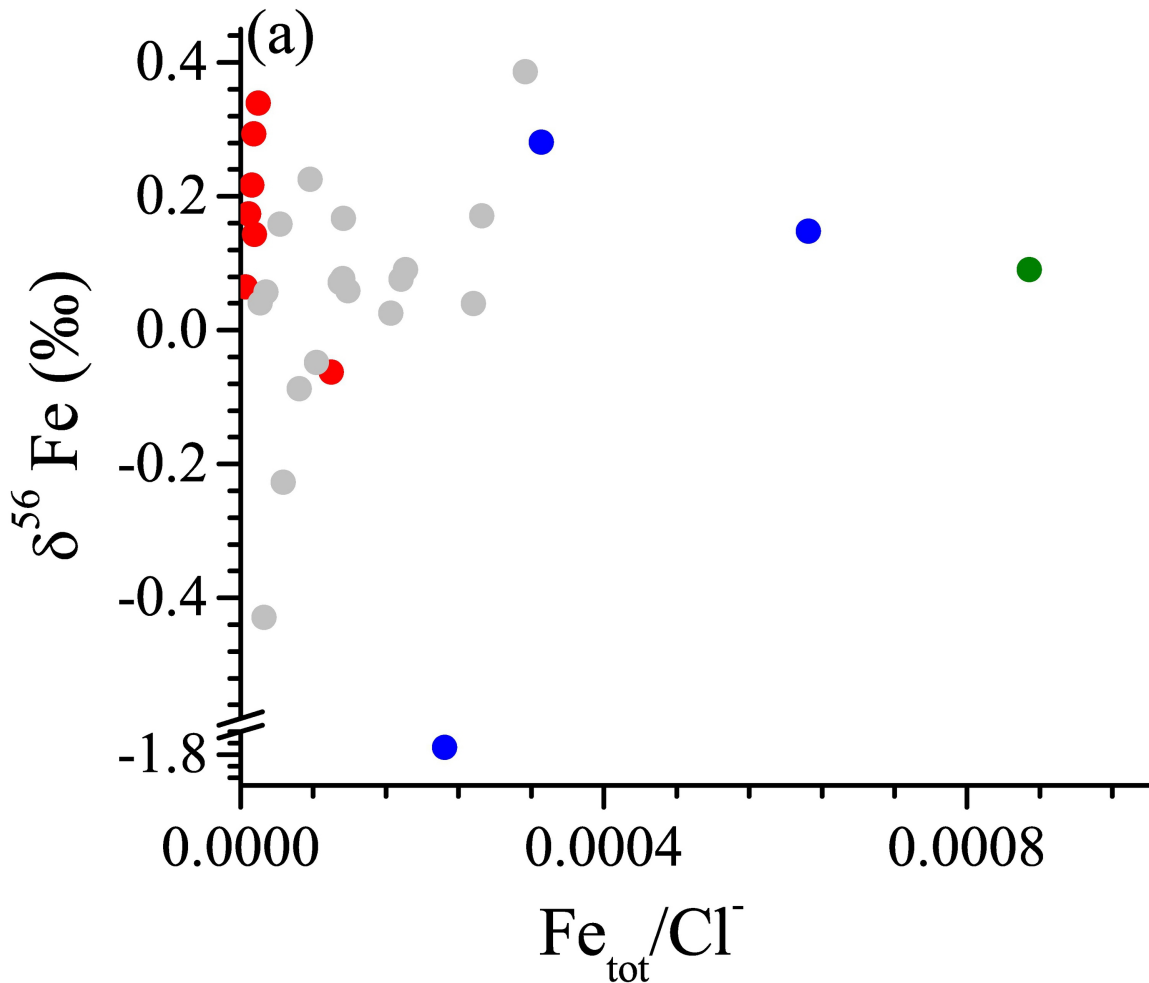


Figure 5

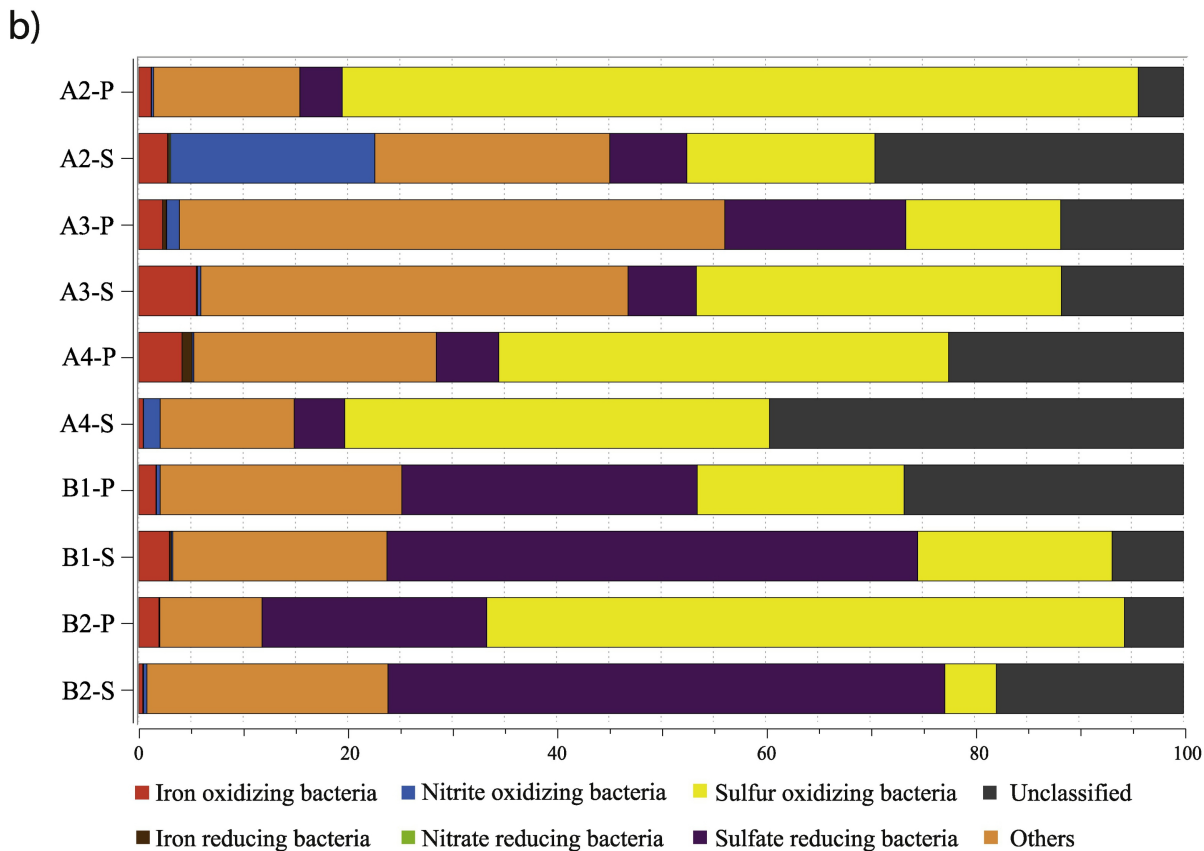
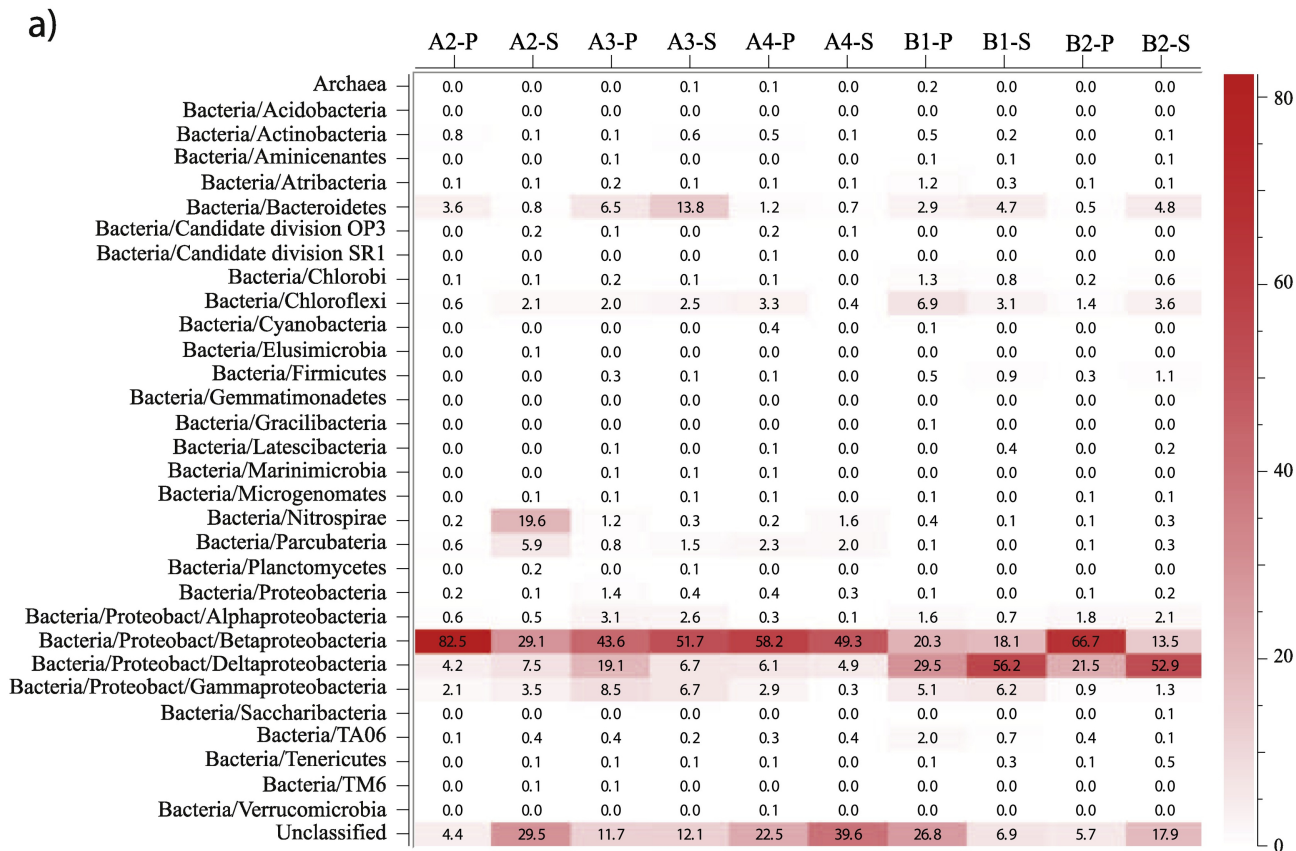


Figure 6

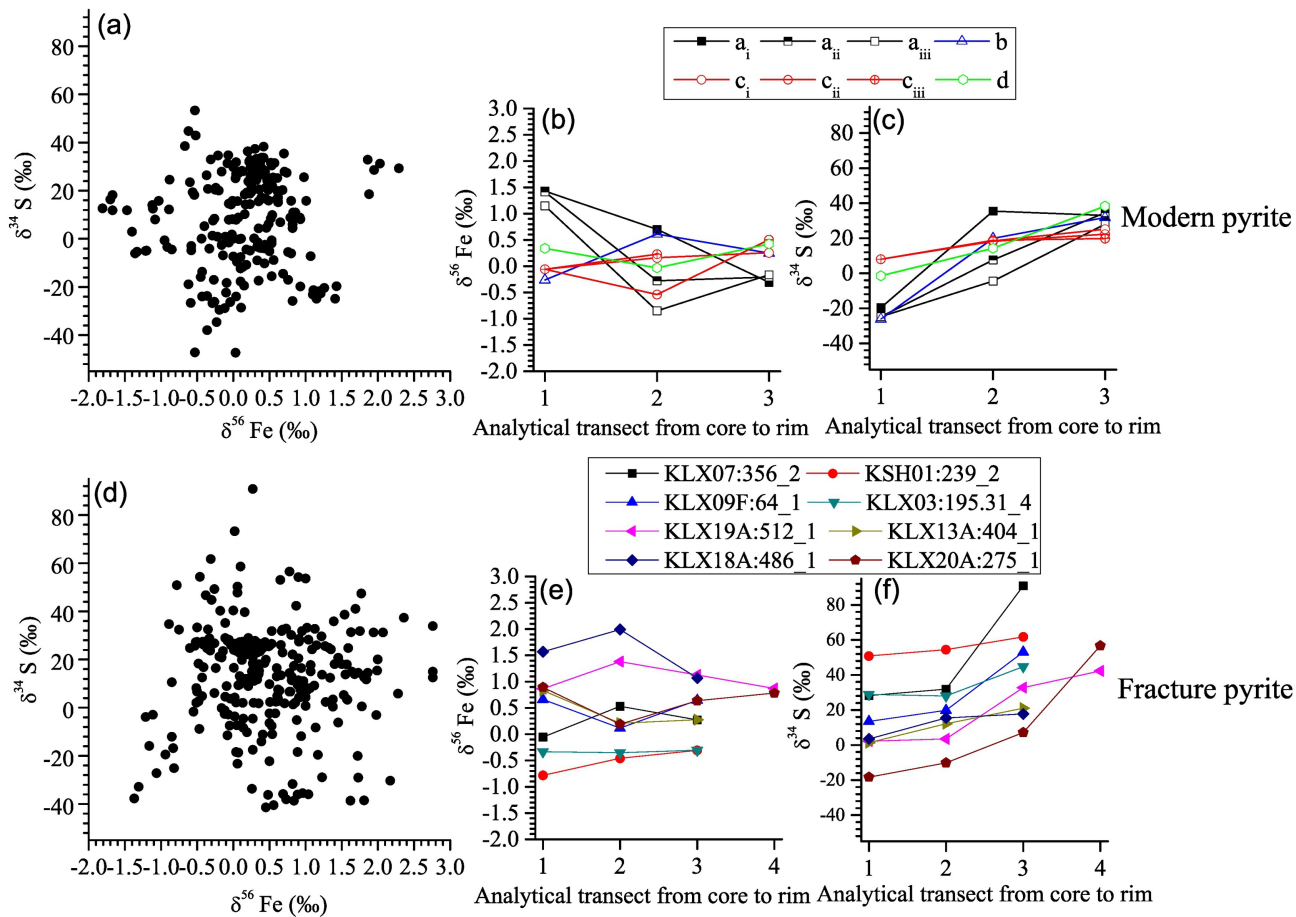


Figure 7

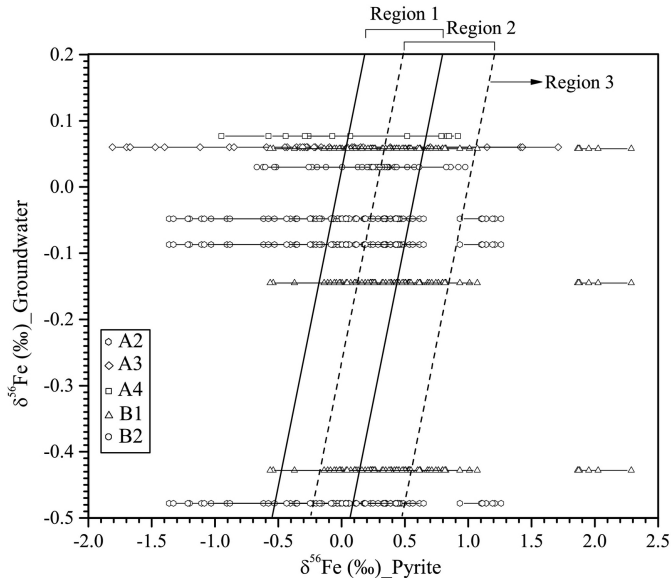


Figure 8